

# Remote sensing of local-dust across the Canadian Arctic

Seyed Ali Sayedain<sup>1</sup>, Norman T. O'Neill<sup>1</sup>, Keyvan Ranjbar<sup>2</sup>, Phillipe Gauvin-Bourdon<sup>3</sup>, Rachel Chang<sup>3</sup>, Patrick L. Hayes<sup>4</sup>, James King<sup>5</sup>

<sup>1</sup>Centre d'Applications et de Recherches en Télédétection, Université de Sherbrooke, Sherbrooke, QC, Canada

<sup>2</sup>Flight Research Laboratory, National Research Council Canada, Ottawa, ON, Canada

<sup>3</sup>Department of Physics and Atmospheric Science, Dalhousie University, Halifax, NS, Canada

<sup>4</sup>Département de chimie, Université de Montréal, Montréal, QC, Canada

<sup>5</sup>Département de géographie, Université de Montréal, Montréal, QC, Canada

Correspondence to: S. A. Sayedain ([seyed.ali.sayedain@usherbrooke.ca](mailto:seyed.ali.sayedain@usherbrooke.ca))

## Abstract.

We investigated the optical and microphysical characterization of High- and sub-Arctic dust events across the Canadian Arctic Archipelago (CAA). Events from local sources (local dust) were first identified and characterized using a combination of ground-based lidar, two AERONET instruments, and passive (MODIS, Sentinel-2, MISR) imagery in the neighbourhood of the High-Arctic Polar Environment Atmospheric Research Laboratory (PEARL) at Eureka, Nunavut (on Ellesmere Island in the northernmost part of the CAA).

The PEARL findings informed the identification and characterization of local dust events over other parts of the CAA using a suite of satellite instruments whose remote sensing (RS) capabilities were complementary to or an extension of the ground- and satellite-based techniques employed at Eureka. The events included plumes emanating from Axel Heiberg Island, just west of Ellesmere Island, Banks Island in the southwest corner of the CAA, Ellef Ringnes Island in the eastern part of the central CAA and Prince of Wales Island / Victoria Island in the central southern CAA. Plume identification, plume source and CM (coarse mode) aerosol optical depth (AOD) retrievals were investigated using a combination of low to high spatial resolution (MODIS to Sentinel-2) color imagery and the MODIS dark target AOD product over water. Plume thickness, height and speed for most of the events were obtained (depending on orbit availability and lack of cloud contamination) from MISR (Multi-angle Imaging Spectro Radiometer) stereoscopic products.

These RS results support an argument for the ubiquitous presence of pan-Arctic, low altitude dust that is typically (away from any strong sources such as mountainous drainage basins) at the lower levels of detectability offered by ground- and satellite-based RS techniques. The ability to RS airborne, near-source, local dust events and characterize dust properties and dynamics of important regions such as the CAA is critical to understanding local dust impacts such as early snow/ice melt and the nucleation role of local dust in the formation of low-altitude clouds.

## 30 **1 Introduction**

31 Local, drainage-flow dust events are recognized as an important source of dust at high latitudes (Bullard et al., 2016) and are  
32 a significant contributor to Arctic and sub-Arctic aerosols in terms of total atmospheric (columnar) dust loads and notably, to  
33 near-surface concentration and attendant surface deposition (Groot Zwaaftink et al., 2016). Meinander et al. (2022) employed  
34 dust-transport simulations supported by recent verification data (including the identification of sources using satellite-based  
35 imagery) to confirm the predominance of high-latitude dust (HLD) sources in terms of snow and ice deposition. O'Neill et al.  
36 (2025) summarized satellite-derived findings of what was likely local dust deposition (with attendant decreases in visually  
37 observed surface reflectance) for a sampling of drainage basin regions in the CAA. Local dust, whose source plumes can  
38 produce quite strong coarse mode<sup>1</sup> (CM) AODs (aerosol optical depths) eventually spread out and/or are deposited to yield  
39 weak, monthly-binned CM AODs (O'Neill et al., 2025 who employ the term DOD [dust optical depths] for the CM AODs  
40 known to be dominated by dust).

41 Dust from Asian deserts can be transported around the world and contributes to the dust load over the Arctic (see for example  
42 Uno et al., 2009). AboEl-Fetouh et al. (2020) argued that there was a small but distinct springtime, pan-Arctic (CM) AOD<sup>2</sup>  
43 contribution of what was likely Asian dust over six AERONET stations spread across the Canadian and northern European  
44 Arctic. They also noted that the particle-volume size distribution (PVSD) associated with those CM AODs showed a peak  
45 radius  $\sim 1.3 \mu\text{m}$ . This feature tends to dominate monthly-binned CM AOD averages in the spring (ibid) while DODs associated  
46 with local sources are likely more prevalent in the summer and fall according to the monthly-binned simulations (Fig. 7) of  
47 Groot Zwaaftink et al. (2016)<sup>3</sup>. Aside from its rather unique temporal signature, Asian dust tends to be concentrated in weak  
48 to moderately strong DOD plumes located in the mid- to upper-troposphere with some evidence of dust deposition during the  
49 period of relatively strong Asian dust events (see, for example, the Fig. 3 Barrow event of Zhao et al., 2022).

50 Local dust particles in the Arctic are known to be strong ice nucleating particles (INPs) that can significantly influence the  
51 dynamics of mixed-phase clouds (ice crystals and water droplets) and their optical and radiative impacts (Xi et al., 2022, Kawai  
52 et al., 2023). The dust plumes lofted into the atmosphere from the Copper River Delta in southern Alaska during late summer  
53 or autumn were, for example, shown to be a major INP source (Barr et al., 2023). Those authors also pointed out that the dust  
54 events can last for many days and extend hundreds of kilometers into the Gulf of Alaska. Tobo et al. (2019) noted that the high  
55 ice nucleating ability of local dust in the Svalbard region of the European Arctic was likely improved by the presence of organic  
56 matter.

---

<sup>1</sup> Roughly speaking, particles of super  $\mu\text{m}$  (radius) size

<sup>2</sup> their CM AODs corresponded to integrations of the retrieved AERONET particle-volume size distribution across retrieval radii ranging from a fixed (interpolated) value of  $0.6 \mu\text{m}$  (Dubovik et al., 2002) to an upper bin edge of  $17.18 \mu\text{m}$  (AboEl-Fetouh et al., 2020 explicitly define the bin centers and the bin edges in their Table S1)

<sup>3</sup> Their source and receptor regions represent broad “cap” areas that are greater than a certain latitude

57 HLD events in the Canadian Arctic and specifically the CAA are rarely monitored and so their properties are, accordingly, not  
58 well characterized: low population density and limited numbers of meteorological stations have resulted in a scarcity  
59 of observations. Persistent cloudy periods and the attendant underuse of RS data have represented significant challenges to the  
60 exploitation of satellite RS data (Bullard et al., 2016). Alternatively, optically thinner clouds and / or surface reflectance  
61 perturbations (such as white froth from waves) could act to contaminate AOD retrievals over water.

62 Satellite imagery at different spatial and temporal resolutions in the polar regions can provide color images of dust events as  
63 well as plume characterization products (including AOD, plume height and thickness, coarse indicators of particle size,  
64 etc.) that help to better characterize local dust. Satellite-based, high spatial-resolution RS data can, for example, enable the  
65 separation of local dust-plume patterns from suspended sediments and phytoplankton blooms in the water.

66 The identification of dust plumes over the Icelandic region using MODIS true color imagery has been reported for events  
67 dating back to 2002 (Arnalds, 2010). Satellite- and airborne-RS of local dust over the Arctic (as summarized by Sayedain et  
68 al., 2023; SDN) include airborne RS of dust over the riverbed, fjord, and coastal regions of Svalbard, sub-Arctic dust plumes  
69 flowing over the Gulf of Alaska (where they are much more readily identified and characterized), and MODIS- and CALIOP-  
70 based identification of dust plumes from Iceland. A local, high-Arctic CM dust plume, induced by the drainage basin dynamics  
71 of Lake Hazen (~ 300 km northeast of Eureka on Ellesmere Island), was identified and characterized by Ranjbar et al. (2021)  
72 using various types of passive and active, satellite-based RS tools adapted to the special case of dust optics and microphysics.  
73 Baddock et al. (2024) provided a detailed analysis of a dust event over Pearly Land, Northern Greenland employing Sentinel-  
74 2 true-color images supported by reanalyzed near-surface wind and temperature data.

75 In terms of ground-based RS, Yang et al., (2020) used Doppler lidar (backscatter and depolarization ratio channels) and  
76 ceilometer profiles, along with CIMEL photometry (the instrument employed by AERONET) to characterize the optical  
77 properties of Icelandic, sub-Arctic dust plumes. Bachelder et al. (2020) reported peak CM radii of ~ 1.63  $\mu\text{m}$  for their measured  
78 near-source particle-mass size distributions (PMSDs) of local dust in the sub-Arctic Ä'äy Chù (Slims River) basin in the  
79 Canadian Yukon. SDN characterized the optical and microphysical properties of Lhù'ààn Mân'<sup>4</sup> dust plumes using CIMEL  
80 and Doppler lidar instrumentation supported by microphysical surface measurements. Their CIMEL- and lidar-derived dust  
81 AODs (which we will refer to as DODs in cases where dust is likely the predominant aerosol) were CM dominated (weaker  
82 fine mode DODs that correlated with the CM DODs were also observed).

83 Kawai et al. (2023) simulated the columnar mass concentrations of local dust in the Arctic in order to lay the groundwork for  
84 their investigations into the strong role of local dust as INP. They employed CALIOP profiles and the CALIOP aerosol subtype  
85 classification product to produce a local-dust Arctic DOD climatology in order to verify the quality of their dust simulations.  
86 Their map of simulated columnar mass abundance of pan-Arctic dust helped contextualize (roughly guide or even semi-  
87 quantitatively validate) our search for dust events in the CAA that would be detectable using satellite-based RS. In general,

---

<sup>4</sup> The Kluane Lake Research Station about 8 km east of the Ä'äy Chù measurement station

88 we expect DODs associated with local dust to be dominated by CM particles (see, for example, the overview given in O'Neill  
89 et al., 2025).

90 The instruments and measurements that we employed in the investigations reported in this paper, reflect a general strategy of  
91 using ground-based microphysical as well as ground-based passive and active RS measurements acquired at the High-Arctic  
92 PEARL observatory as a means of demonstrating the presence of local dust in the PEARL region and then linking, by direct  
93 or indirect means, this information with imagery available from the very frequent overpasses of satellite-based instruments  
94 over a site that is near the tangent circle of all polar-orbiting satellites (and thus the beneficiary of a high density of RS data).  
95 With this type of analysis in hand we sought to support/inform (without the ground-based RS and microphysical sampling  
96 capabilities of the PEARL complex), the purely satellite-based RS and characterization of local dust events in other parts of  
97 the CAA. The motivation for this work was to analyze and help verify / evaluate elements of the large potential trove of  
98 satellite-based dust RS data over the CAA.

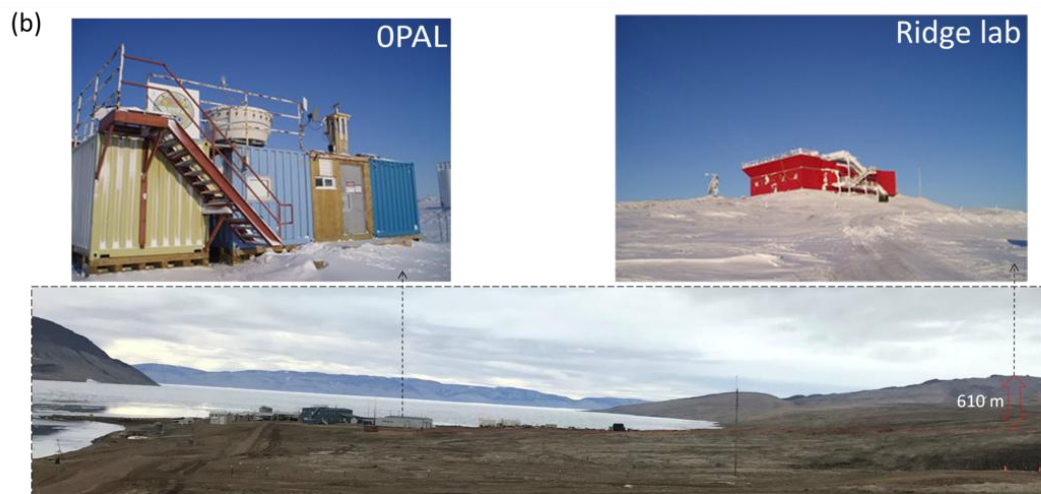
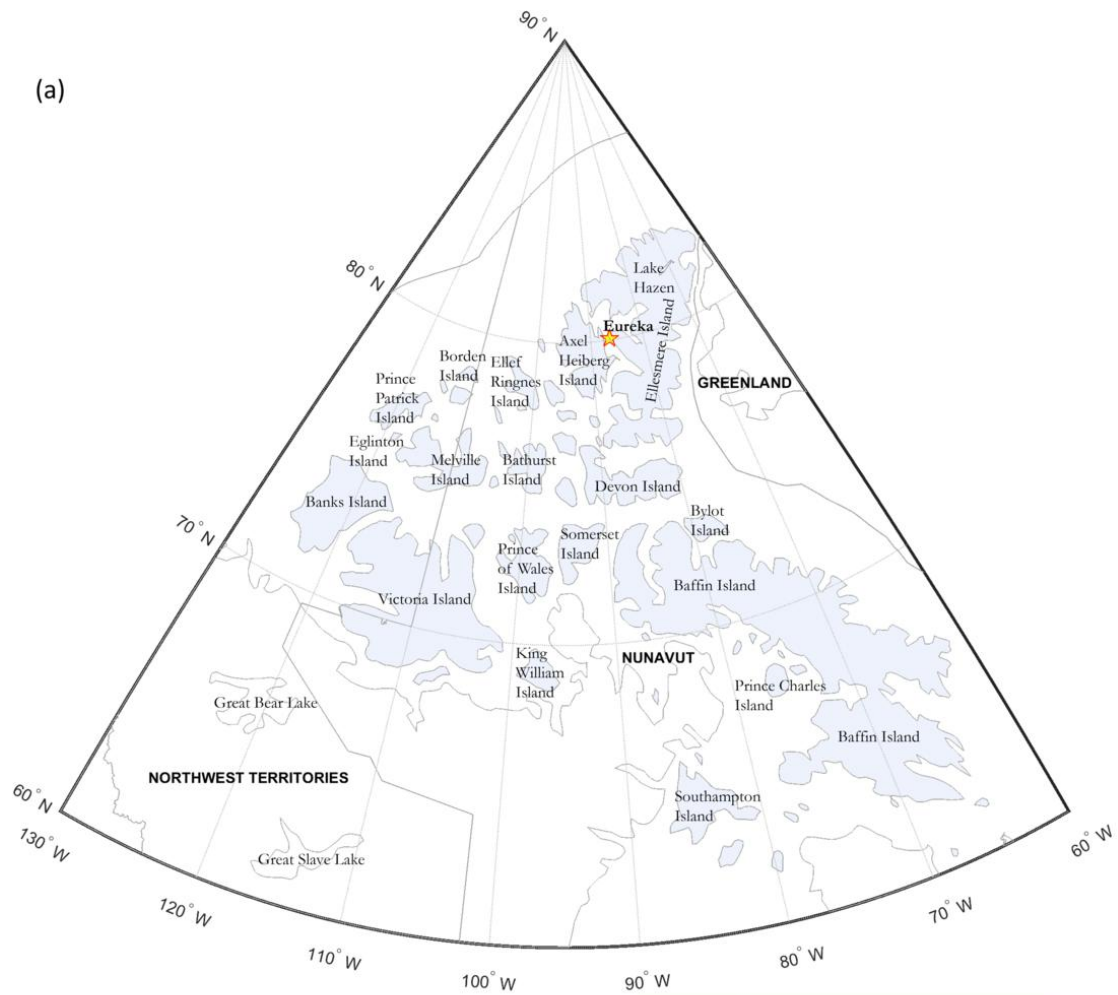
## 99 **2 Study Area**

### 100 **2.1 The Canadian Arctic Archipelago**

101 The CAA extends from the northern (low Arctic) shores of the Canadian mainland to the high Arctic (Fig. 1a). It consists of a  
102 group of approximately 36,000 islands, many of which are covered by ice for much of the year (Adams et al., 2015). Different  
103 local CAA dust events at Eureka on Ellesmere Island, Axel Heiberg Island, Prince of Wales Island, Banks Island, and Ellef  
104 Ringnes Island were investigated as part of this local dust analysis.

#### 105 **2.1.1 The PEARL research complex**

106 The Polar Environment Atmospheric Research Laboratory (PEARL) at Eureka is an important High-Arctic location where  
107 optical and microphysical measurements of gases, aerosols and clouds are conducted on a quasi-continuous basis. The PEARL  
108 complex (indicated by a star on the map of Fig. 1a) includes two atmospheric measurement sites (Fig. 1b): the OPAL (Zero  
109 Altitude PEARL Auxiliary Laboratory) at 5 m ASL, and the Ridge lab at 615 m ASL. The OPAL site and the Ridge lab are  
110 separated by a 15 km-long gravel road.



112 **Figure 1 – (a) The geographical extent of the CAA as indicated by light-blue shading. The PEARL observatory at Eureka, Nunavut**  
113 **is indicated by a yellow star, (b) the PEARL complex showing both the 0PAL (left) and Ridge lab (right) sites (a wide-angle photo**  
114 **of the PEARL complex is below those photos). The nominal (AERONET) coordinates of the 0PAL and Ridge lab sites are,**  
115 **respectively; 79.990° N, 85.939° W at 5 m elevation and 80.054° N, 86.417° W at 615 m elevation.**

### 116 **3 Instrumentation & Methodology**

117 In this section, we present a brief overview of the instruments and measurements employed in our local dust investigations at  
118 the PEARL complex and a summary of the satellite imagery products that we employed over targeted CAA sites in our search  
119 for detectable dust events.

#### 120 **3.1 Sun photometer / sky radiometer**

121 Spectral AOD and almucantar sky radiance measurements were acquired by two automated AERONET CIMEL sun  
122 photometer/sky radiometers (see Giles et al., 2019, for recent details on the CIMEL instrument and the AERONET network).  
123 The Canadian sub-network of AERONET (AEROCAN) is run by Environment and Climate Change Canada (ECCC) in  
124 collaboration with AERONET (Ihab Abboud is the AEROCAN coordinator). The Ridge lab and the 0PAL CIMEL have been  
125 in operation from 2007 to 2019 and from 2007 to the present, respectively<sup>5</sup>. The Ridge lab CIMEL is labeled "PEARL" in the  
126 AERONET database.

127 The CIMEL instruments acquire solar-disk irradiances across eight spectral channels from the ultraviolet (UV) to the short-  
128 wave infrared (SWIR) at central wavelengths ( $\lambda$ ) of 340, 380, 440, 500, 675, 870, 1020, and 1640 nm in a sequence of three  
129 10-second (triplet) observation at a nominal temporal resolution of 3 minutes between triplets (15 min for older CIMEL  
130 versions). Version 3, Level 1.0 AERONET AODs were employed in the analysis (unless otherwise stated). These AOD spectra  
131 yield fine mode (FM) and coarse mode (CM) AODs (the AERONET SDA product at 500 nm wavelength) with pre-cloud-  
132 screened filtering being driven by a ceiling on the variation of the triplets (see Giles et al., 2019, for AERONET processing  
133 details and products) .

134 The CIMELs also acquire (low frequency) AOD spectra and almucantar radiances across four spectral bands (380, 440, 675,  
135 870 nm) at a nominal temporal resolution of 1 hour<sup>6</sup>. Version 3, Level 1.5 (cloud-screened) AOD measurements and associated  
136 almucantar radiances are inverted to yield (what amount to) columnar averages of refractive index and PVSDs.

---

<sup>5</sup> The AERONET database name for "0PAL" is written as "OPAL"

<sup>6</sup> supplemented by 4 additional AOD / almucantar measurement series at solar airmasses of 4, 3, 2 and 1.7 (Sinyuk et al., 2020).

### 137 **3.2 Aerodynamic Particle Sizer Spectrometer**

138 The Aerodynamic Particle Sizer (APS) spectrometer measures both aerodynamic diameter and light-scattering intensity (TSI  
139 Incorporated, 2022). Their basic size distribution product is a largely CM product (52 optical channels with an aerodynamic  
140 particle diameter range between 0.5 to 20  $\mu\text{m}$ ). The chosen temporal bin-sampling frequency was 1 minute. Particle-number  
141 size distributions ( $dN/d\log D$ ) are calculated by dividing the measured number concentration of each bin by its logarithmic  
142 bin size ( $d\log D$ ). PVSD concentrations ( $dv/d\log D$ ) are then expressed in terms of equivalent spherical particles  
143 ( $\frac{4}{3}\pi (D/2)^3 dN/d\log D$ ). CM particle-volume concentrations ( $v_c$ ) are obtained by adding the  $dv = PVSDs \times d\log D$  across  
144 a range of CM channels<sup>7</sup> ( $v_c = \sum_{i=21}^{i=52} dv$ ).

### 145 **3.3 Arctic High Spectral Resolution Lidar**

146 The Arctic High Spectral Resolution Lidar (AHSRL) was deployed at OPAL between August 2005 and June 2010. The AHSRL  
147 employs Doppler-type lidar technology to separate (slow-moving aerosol and fast-moving molecular), velocity-induced  
148 differences in Doppler frequencies. This separation enables the retrieval of particle (aerosol and/or cloud) to molecular  
149 backscatter coefficient ratios that, in turn, allow for the extraction of particle backscatter profiles by the simple expediency of  
150 multiplying by the relatively well-known molecular backscattering profile (see Eloranta's HSRL chapter in Weitkamp, 2005).  
151 The AHSRL provides backscatter coefficient<sup>8</sup> ( $\beta$  with units of  $\text{sr}^{-1} \text{km}^{-1}$ ) and volume depolarization ratio (VDR<sup>9</sup>) profiles of 7.5  
152 m vertical resolution up to 30 km of altitude and inter-sample resolution of 1 minute (Eloranta et al., 2004). The VDR is a  
153 well-known source of information related to the optical separation of FM and CM contributions to the backscatter signal. We  
154 employ that type of information below to make links with CM AODs (DODs) derived from the CIMEL instruments.  
155 The  $\beta$  altitude profiles can be integrated to yield what we refer to as the particulate backscatter optical depth ( $\tau_\beta$ ) whose FM  
156 and CM AOD components are  $\tau_{\beta,f}$  and  $\tau_{\beta,c}$ . If the FM and CM profiles are largely dominated by homogeneous particle types  
157 (like, respectively, FM sulphatic-based pollution particles and CM dust) then their corresponding optical depths are given by  
158  $\tau_f^l = S_f \tau_{\beta,f}$  and  $\tau_c^l = S_c \tau_{\beta,c}$  (where  $S_f$  and  $S_c$  are the lidar ratios [sr] of the FM and CM particle types).

---

<sup>7</sup> from bin (i) = 21 to 52. This bin range corresponds to geometric bin center diameters of  $D = 1.47$  to  $13.66 \mu\text{m}$ . Geometric diameters are taken as the aerodynamic diameter / 1.45 (see, for example, Huang et al., 2021).

<sup>8</sup> What the lidar community refers to as backscatter cross section (but which we have adapted to better fit into the extinction coefficient vocabulary of the radiative transfer community; see, for example, Hansen and Travis, 1974)

<sup>9</sup> For purposes of symbolic brevity, we also employ  $\delta$  to represent VDR in any equation context.

### 159 **3.4 Satellite imagery**

160 MODIS satellite images along with their derived AOD products as well as MISR multi-view images and their AOD, plume  
161 height and plume speed products were employed to investigate a variety of dust events using the contextualizing diversity of  
162 information layers available from the NASA Worldview<sup>10</sup> application. High spatial resolution Sentinel-2 color images from  
163 the Copernicus Browser<sup>11</sup> were also employed on an as-needed basis: they often yielded physical and/or spatio-temporal  
164 insights into local dust behavior that was not obvious in the (comparatively) low-resolution MODIS imagery and products.

#### 165 **3.4.1 MODIS**

166 MODIS multispectral imagers operate on both the descending-orbit (Terra) and ascending orbit (Aqua) satellites at an altitude  
167 of 705 km<sup>12</sup>. MODIS employs 36 spectral bands between 400 nm (UV) and 14.4 μm (thermal-IR) at three different nadir  
168 spatial resolutions of 250 m (bands 1–2), 500 m (bands 3–7), and 1 km (bands 8–36). The sensor has a swath width of 2330  
169 km (cross-track) by 10 km (along track at nadir) and views the entire Earth every one to two days, depending on the latitude  
170 of the orbit line (Justice et al., 2002). The MODIS “true color” RGB images provided by the NASA Worldview application  
171 have a spatial resolution of 250 m (R = Band 1 @ 620–670 nm, G = Band 4 @ 545–565 nm, B = Band 3 @ 459–479 nm).

172 The highest-resolution, 3 km land and ocean (550 nm) AOD products (Terra, MOD04\_3K, and Aqua, MYD04\_3K)  
173 are computed using the Dark Target (DT) algorithms over dark land and ocean targets during daytime overpasses  
174 (Levy et al. 2015a, 2015b). We employed the 3 km data while monitoring the predictions of the 10 km Deep Blue (DB) AOD  
175 product over Arctic land surfaces (Levy et al. 2015c, 2015d) where the DT AOD product was typically sparse or non-existent.  
176 The DT algorithm’s dependence on the presence of dense dark vegetation to achieve its dark pixel threshold over land is rarely  
177 achieved over the Arctic: the DB algorithm was designed to retrieve AOD over surfaces such as deserts or arid lands that are  
178 bright in the visible wavelength spectrum (Sayer et al., 2014). It is tempting to employ this product given that vegetation-  
179 sparse Arctic tundra often satisfies the conditions for the generation of DB AODs. However, it is a largely untested product  
180 over high-Arctic sites (Sayer, 2025) and our investigations showed the presence of frequent AOD plumes (patches) that were  
181 often inordinately coincident with persistently dark reflectance patterns in the imagery. In the end we relied almost exclusively  
182 on the DT retrieval over water surfaces.

183 We employed the MODIS FMF (Fine Mode Fraction) product (Song et al., 2021) as a means of separating out the CM AOD  
184 from the AOD (CM AOD =  $(1 - \text{FMF}) \times \text{AOD}$ ). As indicated above, the DOD is generally expected to be dominated by CM  
185 particles. Sea-spray particles are also CM in nature: however, the unique spatial nature of dust plumes and their land-based  
186 origin largely occluded any possible mixup with sea-salt particles.

---

<sup>10</sup> <https://worldview.earthdata.nasa.gov/>

<sup>11</sup> <https://dataspace.copernicus.eu/browser>

<sup>12</sup> Local-time equatorial crossings of 10:30 a.m. and 1:30 p.m. respectively

### 187 **3.4.2 MISR**

188 The Multi-angle Imaging SpectroRadiometer (MISR), aboard the Terra satellite, acquires images of the same scene at nine  
189 different viewing angles. The imagery ranges from aft- or backward-looking ( $-70^\circ$ ) to fore- or forward-looking ( $+70^\circ$ ) views  
190 in four spectral bands (blue @ 447 nm, green @ 558 nm, red @ 672 nm, and near-infrared @ 867 nm). The “Global Mode”  
191 nadir spatial resolution is 275 m which degrades to 1.1 km for all off-nadir bands except the red band (MISR Handbook, 2000).  
192 The latitude-dependent revisit time is every 2 to 9 days across a 380 km swath (Garay et al., 2020). The stereoscopic nature of  
193 the 9 MISR images enables the extraction of plume height and plume velocity. Both parameters are critical for dust plume  
194 investigations. This was notably, demonstrated by Ranjbar et al. (2021), for the case of a strong local-dust plume over Lake  
195 Hazen (about 330 km northeast of PEARL) that was characterized using MISR, MODIS, CALIOP and CloudSat data. More  
196 detailed information on MISR stereoscopic height and wind speed retrievals and the algorithm used to generate these products  
197 (the MISR Interactive eXplorer or MINX algorithm) can be found in Nelson et al. (2013), who also provide case studies of  
198 plume height and wind speed retrievals for smoke, dust, and cloud.

199 It was known, from its earliest conception, that the multi-angle feature of MISR would facilitate the extraction of aerosol  
200 parameters given their spatial invariance relative to the typically high frequency spatial variance and differing spectra of surface  
201 reflectance (see, for example, the definitive overview of Martonchik et al., 1998). The specific stereoscopic capabilities of  
202 MISR enable, in turn, the detection of aerosol or cloud plumes and the computation of their optical depth (see, for example,  
203 Kahn et al., 2007, for the case of dust, smoke and volcanic plumes at the 17.6 km atmospheric processing resolution). More  
204 recent versions of the MISR processing chain included a 4.4 km resolution, near real time, V23, Level 2 AOD product (Witek  
205 et al., 2021) whose AODs are reported at the standard reference wavelength of 550 nm (ibid). We employed both the MISR  
206 plume height and AOD products in our investigations of local-dust events across the CAA.

## 207 **4 Results & Discussion**

208 Our results are reported in two subsections: 4.1- Analysis of dust events at Eureka and 4.2- Satellite-based RS of local dust  
209 events across the CAA. Our goal is to demonstrate how an experienced-based local dust narrative can be built using the ground-  
210 based optical and microphysical measurements of dust plumes in the Eureka region while underscoring what can be achieved  
211 using satellite-based RS data that is informed, as much as possible, by the ground-based and satellite-based results at Eureka.

### 212 **4.1 Analysis of dust events at Eureka**

213 We carried out a purely optical analysis comparing CIMEL and AHSRL data<sup>13</sup> in order to investigate certain optical dynamics  
214 that were consistent with the apparent presence of dust particles at low elevations between OPAL and the Ridge lab. In a

---

<sup>13</sup> over the extended period that the two data sets were mutually available (August 2005 to June 2010)

215 different sequence of aerosol events, the OPAL CIMEL AOD measurements and in situ APS PVSDs shared a common  
216 measurement period from July 9 to September 20, 2018. These two periods were an important focus of our ground-based  
217 analysis at the PEARL sites. The correlation between different independent datasets was a key aspect of a multi-pronged  
218 strategy to provide evidence of Arctic dust events whose RS detectability can be generally characterized as weak to marginal  
219 (O'Neill et al., 2025).

#### 220 **4.1.1 Passive vs active (ground-based) optical analysis at Eureka**

221 Potential dust events over the August 2005 to June 2010 period (the duration of AHSRL measurements at OPAL) were  
222 investigated by looking for low-altitude, large-amplitude VDR events whose derived CM AODs were correlated with the  
223 OPAL CM AOD ( $\tau_c^O$ ) and not correlated with the PEARL CM AOD ( $\tau_c^P$ ) (if the plumes were found to be largely below the  
224 PEARL\_CIMEL elevation of 615 m). The AHSRL CM AODs ( $\tau_c^L$ ) were obtained by integrating CM lidar backscatter  
225 coefficient ( $\beta_c$ ) profiles associated with VDR values greater than a particular threshold ( $\delta_{thr}$ ) (from the OPAL to Ridge lab  
226 elevations) and employing prescribed FM and CM lidar ratios. The reader is directed to Appendix A1 for a discussion of the  
227 FM / CM attributions between the OPAL and PEARL CIMELs and for temporal resampling details (the resampling of  $\tau_c^P$  and  
228  $\tau_c^L$  measurements to  $\tau_c^O$  times). The theoretical VDR-driven FM / CM attributions for the lidar are defined in Appendix A2.

229 We analyzed the AHSRL profile statistics of 7 events that we claimed to be dust events in Section A3.2. The impact of varying  
230 the FM / CM attribution threshold of the VDRs (the value of  $\delta_{thr}$ ) is detailed in Appendix A3.3<sup>14</sup>. We eventually determined  
231 that a 5% VDR threshold for separating CM and FM optical depths was a reasonable compromise. The AHSRL profile details  
232 as well as the corresponding derived values of  $\tau_c^L$ ,  $\tau_c^O$ ,  $\tau_c^P$ , and the OPAL minus PEARL difference ( $\Delta\tau_c$ ) are shown in Figures  
233 S1a to S7a<sup>15</sup> while the summary (profile- and event-integrated) VDR statistics for those lidar profiles are given in Figures S1b  
234 to S7b of the same file (with the overarching VDR statistics being given in the table of Fig. S8). A brief overview of those  
235 overarching statistics is given in Section A3.2.

236 Figure 2 shows the calculated cloud-screened CM AODs during the apparent dust event of July 23, 2007 (what we call Event  
237 5). We chose it to illustrate the key elements in support of our dust plume detection claims. The  $\tau_c^L$  and  $\tau_{c,1.5}^O$  values show the  
238 high frequency variations that we argue are due to near surface dust. The (high frequency) similarities between the  $\tau_c^L$  and  $\tau_{c,1.5}^O$   
239 “spikes” (coupled with the low frequency unresponsiveness of  $\tau_{c,1.5}^P$  to those spikes) are coherent with an argument for the  
240 presence of a weak, low-altitude dust event. The standard deviation (std) of  $\tau_{c,1.5}^O$  is generally significantly larger than the std of  
241  $\tau_{c,1.5}^P$  (this disparity amounts to a quantitative verification of the relative unresponsiveness of  $\tau_{c,1.5}^P$ ).

242 The  $\tau_c^L$  vs  $\tau_{c,1.5}^O$  intra-event statistics show marginal to moderately large correlation coefficients (R values from 0.41 to 0.64)  
243 for each of the seven events while the inter-event correlation coefficient for the ensemble of seven events was significant (R =

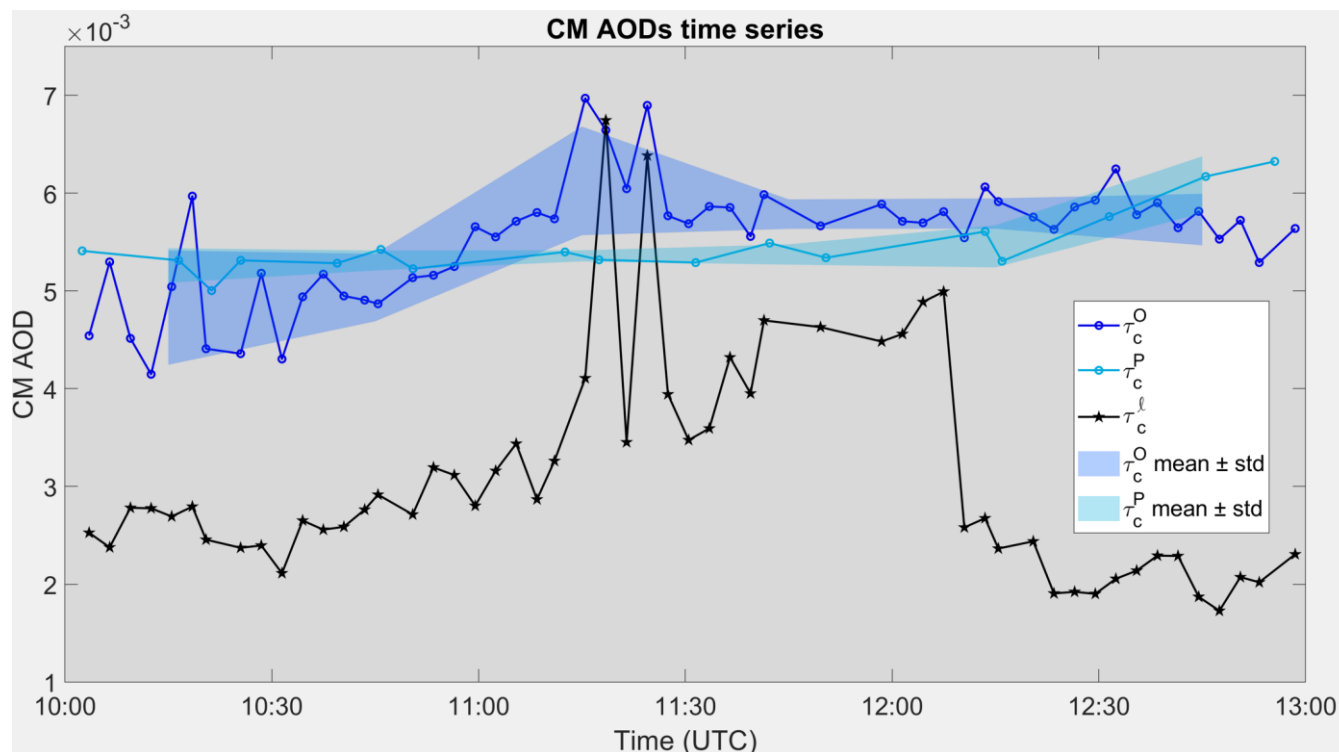
---

<sup>14</sup> Appendix A3.1 is a discussion of how we filtered (weighted) out severe outliers that could appear in the VDR profiles

<sup>15</sup> Supplementary PowerPoint file “AHSRL\_CIMEL\_event\_profiles”

244 0.78). The complete ensemble of individual CM AOD measurements in August and July 2007 show diurnal examples of what  
 245 we determined to be largely dust-free conditions in the 0PAL to PEARL layer. A particular example on July 19, 2007, occurred  
 246 in the presence of very clear background columnar conditions above the 0PAL and PEARL CIMELs<sup>16</sup>: it was thus an explicit  
 247 example of clean background conditions that could be used as reference for declarations of time-varying dust events in the  
 248 layer between the two events.

249  
 250



251  
 252

253 **Figure 2 – Level 1.5 (cloud-screened) CM AOD time series of the July 23, 2007, dust event (Event 5 of our 7 dust events) for the**  
 254 **CIMELs at 0PAL ( $\tau_{c,1.5}^O$ ) and PEARL ( $\tau_{c,1.5}^P$ ) as well as the 0PAL AHSRL ( $\tau_c^l$ ) (altitude range of 5 to 615 m). The  $\delta_{thr}$  value for**  
 255 **separating CM and FM AODs was 5%.  $\tau_{c,1.5}^O$  should, normally, be greater than  $\tau_{c,1.5}^P$  but the nominal CIMEL accuracy of  $\sim 0.01$  /**  
 256 **airmass (for both the 0PAL and PEARL CIMELs) is a key factor in the absolute comparison of these very small CM AOD values.**

<sup>16</sup> Across that layer we found  $\Delta\tau_c^l$  and  $\Delta\tau_c^O$  to be quite small ( $<\sim 0.0003$ ) and  $<\sim 0.0002$  respectively).

257 The solid, blue-toned bands show the running standard deviation (std) about the running mean over 30-minute intervals with the  
258 first-interval mid-point starting at 10:15 UTC<sup>17</sup>.

#### 259 4.1.2 Optical vs microphysical (ground-based) analysis at Eureka

260 Figure 3 encapsulates the analysis that we carried out in the comparison of the CIMEL CM AODs and APS  $v_c$  values associated  
261 with an event that we argue was a significant dust event at Eureka. The simultaneous rise of the APS  $v_c$  values and the  $\tau_{c,1.5}^O$   
262 time series after 20:30 UTC in Fig. 3c and 3d are likely the start of a CM-aerosol event which this and other evidence (see  
263 Section 4.1.3) suggests was a dust event. The zoomed Fig. 3d shows a rather remarkable  $\tau_{c,1.5}^O$  vs  $v_c$  correlation with departures  
264 from that correlation in the neighbourhood of  $\tau_{c,1.5}^O$  and  $v_c$  peaks at, respectively,  $\sim 21:30$  and  $00:30$  UTC (the former could be  
265 ascribed to very thin cirrus clouds that we failed to detect in any satellite data while the latter could be the result of a very  
266 spatially-variable dust plume). During this particular event, two large temporal spikes were eliminated from the Level 1.0  
267 retrievals by the AERONET temporally-driven (Level 1.5) cloud-screening algorithm (the Level 1.0 AERONET product of  
268 “Coarse AOD” can include CM cloud particles as well as CM aerosols). During this particular event, two large temporal spikes  
269 were eliminated from the Level 1.0 retrievals by the AERONET temporally-driven (Level 1.5) cloud-screening algorithm.  
270 Supporting data for this elimination<sup>18</sup> is presented in Figures S9 to S11 where we demonstrate that the Level 1.0 CM AOD  
271 spikes represent cirrus clouds that temporarily fouled the CIMEL sun-pointing FOV as determined using the MISR sensor.<sup>19</sup>  
272 The inferred approximate position of a smaller-radius AERONET PVSD peak in Fig. 3a and the APS peak in Fig. 3b (the cyan  
273 curves at 21:00 UTC) suggests a common mode peak  $\sim 1.3 - 1.5 \mu\text{m}$  (with the AERONET peaks at radii  $\gtrsim 6 \mu\text{m}$  being outside  
274 the radius range of the APS). The  $1.3 - 1.5 \mu\text{m}$  peak radius is  $\sim 1.3 \mu\text{m}$  AERONET inversion peak reported by SDN in their  
275 analysis of local dust at the Kluane Lake<sup>20</sup> AERONET station in the Canadian Yukon (while the  $6 \mu\text{m}$  AERONET peak is near  
276 the upper limit of the reported KLRS peak radius range from  $\sim 4$  to  $7 \mu\text{m}$  for the 5 largest CM AOD cases; see Fig. 9 of that  
277 paper). However, the KLRS CM AODs were  $\sim 2$  to 14 times the CM AODs of the event shown in Fig. 3c (after the onset of  
278 the significant rise around 20:30 UTC for which the CM AODs are  $\sim 0.006$  to  $0.016$  or a  $\Delta(\text{CM AOD}) \sim 0.01$ ). In general, dust  
279 plumes in the Lhù’àn Mân’ region (associated with drainage basins of significantly greater relief than the region of Eureka)  
280 demonstrated a CM AOD domination relative to the dust plumes that we claim to have found at OPAL (Fig. 3c).

---

<sup>17</sup> We produced these bands to focus on the high frequency differences between  $\tau_{c,1.5}^O$  and  $\tau_{c,1.5}^P$  (to avoid the standard deviation contributions of more low frequency variations)

<sup>18</sup> beyond the support provided in the AERONET literature for the efficacy of their cloud screening algorithm

<sup>19</sup> The MISR multi-angle (stereoscopic) capabilities permitted an estimate of the time that the roughly 8 km altitude cirrus cloud (located over Axel Heiberg Island) incited a spike in the Level 1.0 CM AOD.

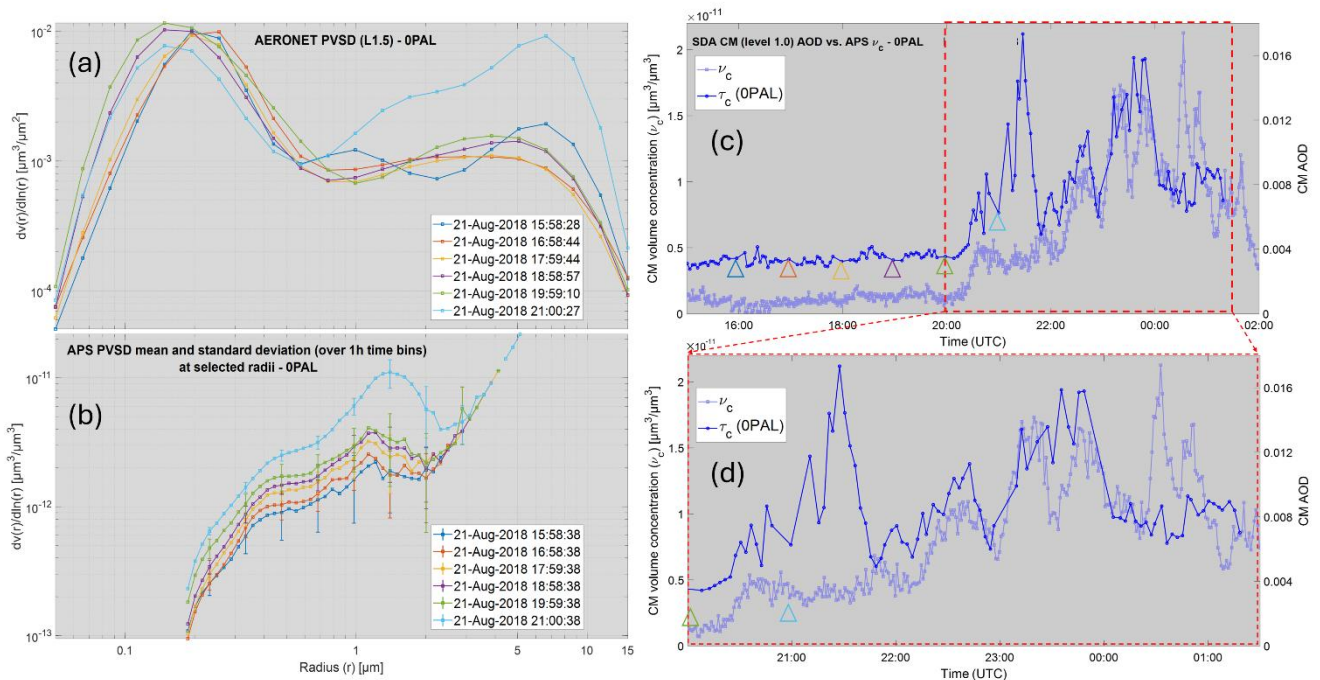
<sup>20</sup> This is the name AERONET ascribed to the CIMEL of the Lhù’àn Mân’ region. SDN referred to the AERONET CIMEL measurements being made at KLRS (Kluane Lake Research Station): KLRS is the acronym that we will associate with the “Kluane Lake” CIMEL

281 SDN speculated that the smaller CM (1.3  $\mu\text{m}$ ) AERONET-inversion peak was more likely ascribable to springtime Asian dust  
282 (while noting that the PVSDs measured with the TSI Optical Particle Sizer (OPS) device at KLRS showed no distinguishable  
283 peak that was comparable with the 1.3  $\mu\text{m}$  AERONET-inversion peak). However, the results presented in Fig. 3b suggest a ~  
284 1.4  $\mu\text{m}$  (small CM) APS peak that is clearly not due to springtime Asian dust (and thus could be ascribable to  
285 phenomenologically different dust PVSDs and CM AODs than those of the much more dynamic and optically strong KLRS  
286 site).

287 We believe that (i) the levels of PVSD-shape correspondence found between the AERONET and APS PVSDs as well as the  
288 higher-frequency temporal correspondence between the AERONET CM AOD values and the APS  $\nu_c$  values and (ii) the purely  
289 optical low-level plume evidence presented above for the July 23, 2007 case (the correspondence between  $\tau_c^o$  and  $\tau_c^l$ ), lend  
290 credence to a claim of having measured, two independent low-level and optically weak (local) dust events at the Eureka OPAL  
291 site (the CIMEL  $\Delta(\text{CM AOD})$  increases during both events were respectively  $0.007 - 0.004 = 0.003$  and  $0.016 - 0.006 = 0.010$ ).  
292 The detection of such optically weak events (which effectively amount to lower limits of precision in ground-based dust AOD  
293 detectability) help to inform (appreciate certain limitations of) any satellite-based (CM AOD) search for optically detectable  
294 local dust events across the CAA. In the first instance, such weak events would seem to be detectable from a satellite sensor  
295 such as MODIS whose nominal precision appears to be significantly smaller<sup>21</sup>. However, MODIS AOD precision is clearly an  
296 excessively optimistic (out of context) statement since that (coarse numeric scale) precision estimate in the presence of very  
297 small AODs would, no doubt, dramatically change (not to mention the fact that the nominal accuracy of the 3 km MODIS  
298 product ( $\pm 0.04$ ) is much larger than the nominal precision).

---

<sup>21</sup> A nominal precision of  $0.04 \times \Delta\text{AOD}$  which for our 2018 CM AOD range yields  $0.04 \times 0.01 = 0.0004$  (i.e.  $0.04 \times \Delta\text{AOD}$  for the best precision case of the 3 km DT over the open-ocean AOD product; Remer et al., 2013).



299

300 **Figure 3 – (a) AERONET inversion PVSDs for the claimed dust event of August 21, 2018, (b) APS hourly-averaged PVSDs at the**  
 301 **times of the AERONET PVSDs (with standard deviations shown as error bars). Note that the APS points beyond ~ 3 μm radius**  
 302 **were either superimposed and/or free of counts in a given bin (c) SDA Level 1.5 CM AOD ( $\tau_{c,1.5}^0$ ) and APS  $v_c$  time series and (d) a**  
 303 **zoom of (c) at the claimed time of the dust event. The triangles shown in (c) indicate the approximate time of the AERONET and**  
 304 **APS PVSDs (color coded to match the colors of the 6 PVSD cases in (a) and (b)). The original high-frequency 3D (1 minute sample**  
 305 **frequency) time series of APS PSDs are available upon request from the authors.**

### 306 4.1.3 Satellite imagery versus ground-based measurements at Eureka

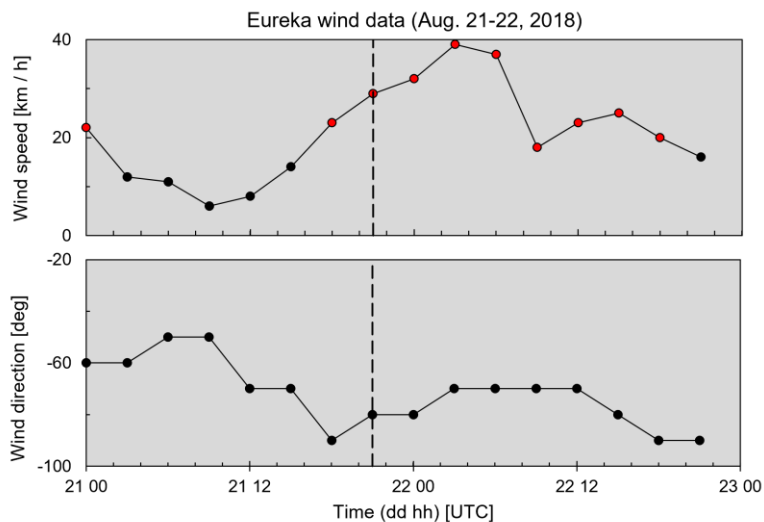
307 The synchronicity between the CM APS  $v_c$  and the  $\tau_{c,1.5}^0$  time series on August 21, 2018 (after 20:30 UTC) coupled with  
 308 evidence of what were likely dust plumes over Eureka Sound (notably weak, grey-white plumes that appear to stretch across  
 309 Eureka Sound<sup>22</sup> at and south of the entrance of Slidre Fjord) provide regional evidence for the possibility of a very weak dust  
 310 event at 0PAL (that was probably incited by the strong (generally north to south) winds of Figure S12 as they travelled over  
 311 the Fosheim Peninsula landmass north of 0PAL). While Sentinel-2 clearly sees apparent dust plumes in Eureka sound (that

<sup>22</sup> See Figures S12 and S13 in the supplementary PowerPoint file “Satellite\_Analysis”. The high spatial resolution (10 m pixels) of the Sentinel-S2A image and the overlain wind-vector field of Fig. S12 along with the blinking Sentinel-S2A images of 19:49 and 20:40 UTC acquisition times, suggest that dust plumes in Eureka Sound likely originated from the barren western slopes of Axel Heiberg Island.

312 MODIS AOD imagery suggests is  $\lesssim 0.03^{23}$ ) even the Sentinel-2 imagery, would likely not detect a sub 0.01 CM AOD (the  
313 post 20:30 UTC  $\tau_{c,1.5}^0$  OPAL CM AOD values of Figures 3c and 3d): the explicit image evidence for weak plumes over or near  
314 the OPAL site is ambiguous at best.

315 Figure 4 shows the temporal variation of the Eureka wind speed ( $ws$ ) and wind direction for Aug. 21 and 22. The rapid increase  
316 at  $\sim 21:00$  UTC in the  $v_c$  and  $\tau_{c,1.5}^0$  time series of Fig. 3c is within the period of significantly high-amplitude  $ws$  values from  
317 18:00 Aug. 21 to 18:00 Aug. 22 (the red-filled points of Fig. 4). This behavior is broadly consistent with CARRA (Copernicus  
318 Arctic Regional Reanalysis) near-surface simulations in the neighbourhood of Eureka Sound to the west of OPAL (the region  
319 of the Aug. 21 dust plumes in the Sentinel-2 image of Fig. S12). We would argue, based on the CARRA spatio-temporal  
320 simulations of generally weaker  $ws$  values at 18:00 UTC to generally stronger values at 21:00 UTC over the Eureka Sound /  
321 OPAL region<sup>24</sup>, that a significantly strong regional wind event<sup>25</sup> incited the Eureka Sound Aug. 21 dust plumes and the attendant  
322  $v_c$  and  $\tau_{c,1.5}^0$  increases near OPAL (the latter plumes likely being induced by northerly winds traversing the slopes of the  
323 Fosheim Peninsula).

324



325

326 **Figure 4 – Temporal variation of the wind speed and wind direction for Aug. 21 and 22, 2018 (data from the ECCC “Eureka Climate”**  
327 **station very near OPAL). The wind direction is defined as the direction that the wind is coming from relative to the station meridian.**  
328 **Positive and negative wind directions refer to CW and CCW angular departures from the meridian. The red-filled points indicate**  
329 **wind speeds that are above the mean + standard deviation ( $15.5 + 2.5 = 18$  km / h) value of the Eureka (August) windspeed**

<sup>23</sup> Very spatially coarse AOD pixels of 3 km resolution: Eureka Sound is  $\lesssim 3$  MODIS-AOD pixels in width

<sup>24</sup> as per Figures S32g and S32h of the Supplementary PowerPoint file “CARRA\_wind\_simulations”

<sup>25</sup> Roughly (qualitatively) lasting from 18:00 Aug. 21 (Fig. 32g) to 06:00 Aug. 23 (Fig. 32s).

330 climatology reported in Fig. 5 of Lesins et al. (2010). The dashed vertical line shows a time (21:00 UTC) that is representative of the  
331 significant rise in CM AOD ( $\tau_{c,1.5}^0$ ) and APS  $v_c$  values in Fig. 3.

## 332 4.2 Satellite-based RS of local dust events across the CAA

333 We employed satellite-based RS to investigate potential dust events over CAA sites where there was no ground-based sensors.  
334 Our goal here was to gain more insight into satellite-based RS capabilities in different types of Arctic environments. A strong  
335 motivation for the CAA analysis was our belief that satellite-based dust RS findings over a variety of CAA sites would help  
336 build confidence in the satellite-based RS of dust events in general and weaker dust events in particular. Each one of our dust  
337 event cases below includes a small CAA map with the position of the event indicated by a green star.

### 338 4.2.1 Large-scale dust event in the northern part of the CAA

339 Figure 5a shows an Aqua true color image<sup>26</sup> of a dust plume that appears to originate from Axel Heiberg Island<sup>27</sup> and flow  
340 along the open water of Eureka Sound and Greely Fjord. The thumbnail images of Figures 5b and 5c show respectively, the  
341 MODIS-Aqua AOD and CM AODs (3 km resolution product) superimposed on the color image. Figure S14a<sup>28</sup> shows a zoom  
342 of the Aqua color image blinking with the AOD and CM AOD products alongside a map of the region (we recommend looking  
343 at such zooms for details). The plume is most evident as it crosses Greely Fjord along its northeastward path and then appears  
344 to veer northwestward towards the coast of the Svartfjeld Peninsula. This flow pattern is generally supported by the surface  
345 *ws* vector field of Fig. S14b (including a final CCW turning (backing) in Greely Fjord followed by a CW turn (veering) of the  
346 dust plume towards Svartfjeld Peninsula<sup>29</sup>). The CM AOD values of Fig. S14a show a spatial pattern that includes a band of  
347 moderately stronger CM AOD values which are coherent with the northeast-flowing spatial pattern of greyish intensity  
348 variations in the true-color image (less evident but still notable is the CM AOD and greyish-intensity pattern matching of the  
349 weaker plume that has veered in the northwesterly direction). The CM AOD values vary from extremes of  $\sim 0.02$  to 0.31 (AOD  
350 extremes of 0.06 to 0.42).

351

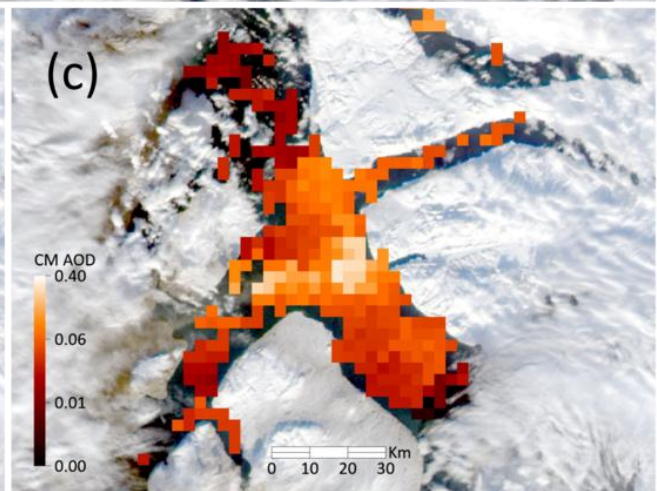
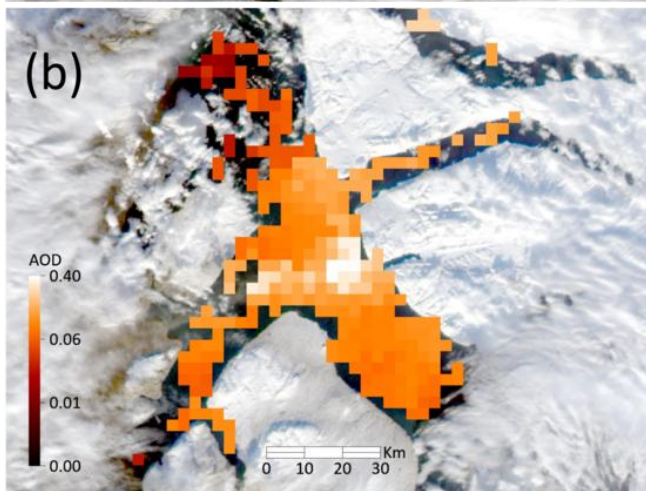
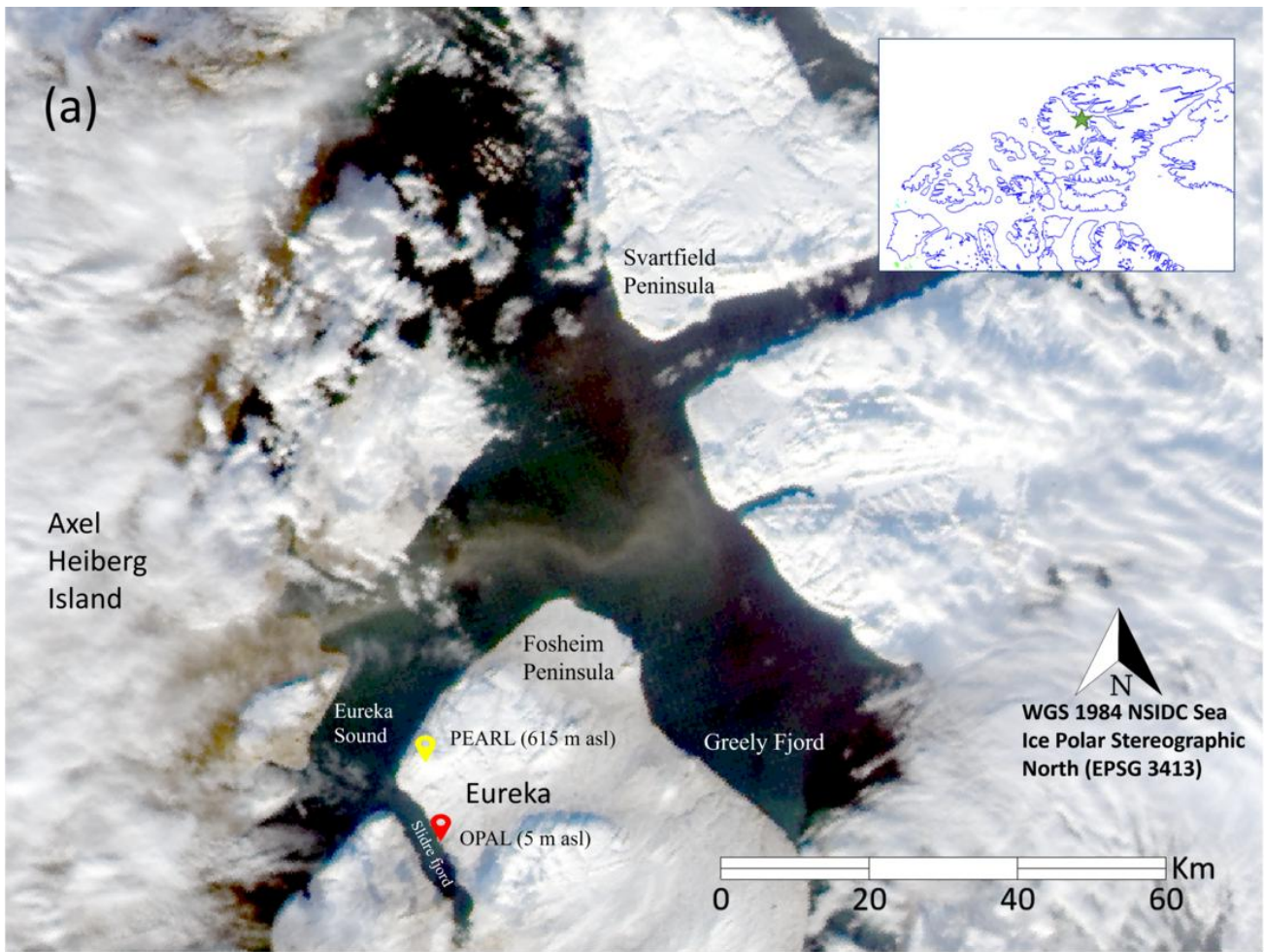
---

<sup>26</sup> Acquired at 15:20 UTC (late morning local time) on September 8, 2020

<sup>27</sup> it appears to be emanating from the largely barren drainage basin whose watershed empties into Eureka Sound (see Fig. S15 for details).

<sup>28</sup> Supplementary PowerPoint file “Satellite\_Analysis”

<sup>29</sup> There are no MINX (MISR) plume height or speed retrievals to report because the plume was basically obscured by clouds at the MISR orbit time of 19:50 UTC.



353 **Figure 5 – (a) MODIS Aqua true color image acquired at 15:20 UTC on Sept. 8, 2020, (b) and (c) MODIS Aqua AOD product and**  
354 **derived CM AOD products respectively (superimposed on the true color image: see Fig. S14a for a detailed (zoomed) overlain**  
355 **comparison of (a), (b), and (c)). See Section 3.4.1 above for the expression relating CM AOD to AOD.**

#### 356 **4.2.2 Dust event in the central southern part of the CAA**

357 Figure 6a shows a (Sept. 26, 2015) MODIS-Terra, true color image of local dust plumes apparently emanating from Prince of  
358 Wales Island (in the central southern part of the CAA) and moving in a northwesterly direction towards Victoria Island (image  
359 acquired at 19:10 UTC). The true color image, along with the MODIS AOD products of Figures 6b and 6c, supported by the  
360 MISR stereoscopic multi-look animation (see Fig. S16<sup>30</sup> and its caption for details) reaffirm the presence of dust plumes  
361 flowing in a northwesterly direction. The color image and MODIS AOD products of Fig. 6 (see Fig. S17 for greater detail)  
362 support a claim of distinct individual dust plumes. The CM AOD and AOD values of the plumes (whose spatial variation is  
363 visually coherent with the variations of the plume-like structure seen in the color image) vary respectively, across extremes of  
364 0.02 to 0.56 and 0.06 to 0.73). The landcover map (Fig. S18) shows a 20-km wide barren region which appears to be the  
365 dominating influence as the source of the dust plumes (judging by the color image combined with the MODIS AOD product).  
366 A sampled MISR trajectory in the direction of the dust plume (the orange-colored trajectory on the MISR color image of Fig.  
367 7a) shows wind-corrected plume height along that trajectory while Figures 7b and 7c show, respectively, plume heights as a  
368 function of trajectory-sample number and the plume heights histogram. The analogous pair of trajectory and histogram graphs  
369 for plume speed are shown in Figures 7d and 7e. The average MINX (MISR) plume height  $\pm$  its standard deviation is  $298 \pm$   
370  $230$  m ASL<sup>31</sup>. The mean and standard deviation of the MISR wind (plume) speed histogram ( $\langle ws \rangle \pm \sigma(ws) = 75 \pm 24$  km  
371 / h or  $54 \pm 17$  km / h when normalized to near surface conditions<sup>32</sup>). This  $\langle ws \rangle$  value is  $\sim$  the 19:00 UTC Sept. 26, 2015  
372 Stefansson Island met station  $ws$  value of 49 km / h and  $\sim$  3-times the (2002 – 2024) Stefansson Island climatological mean  
373 for the month of September ( $17.7 \pm 10.9$  km / h).

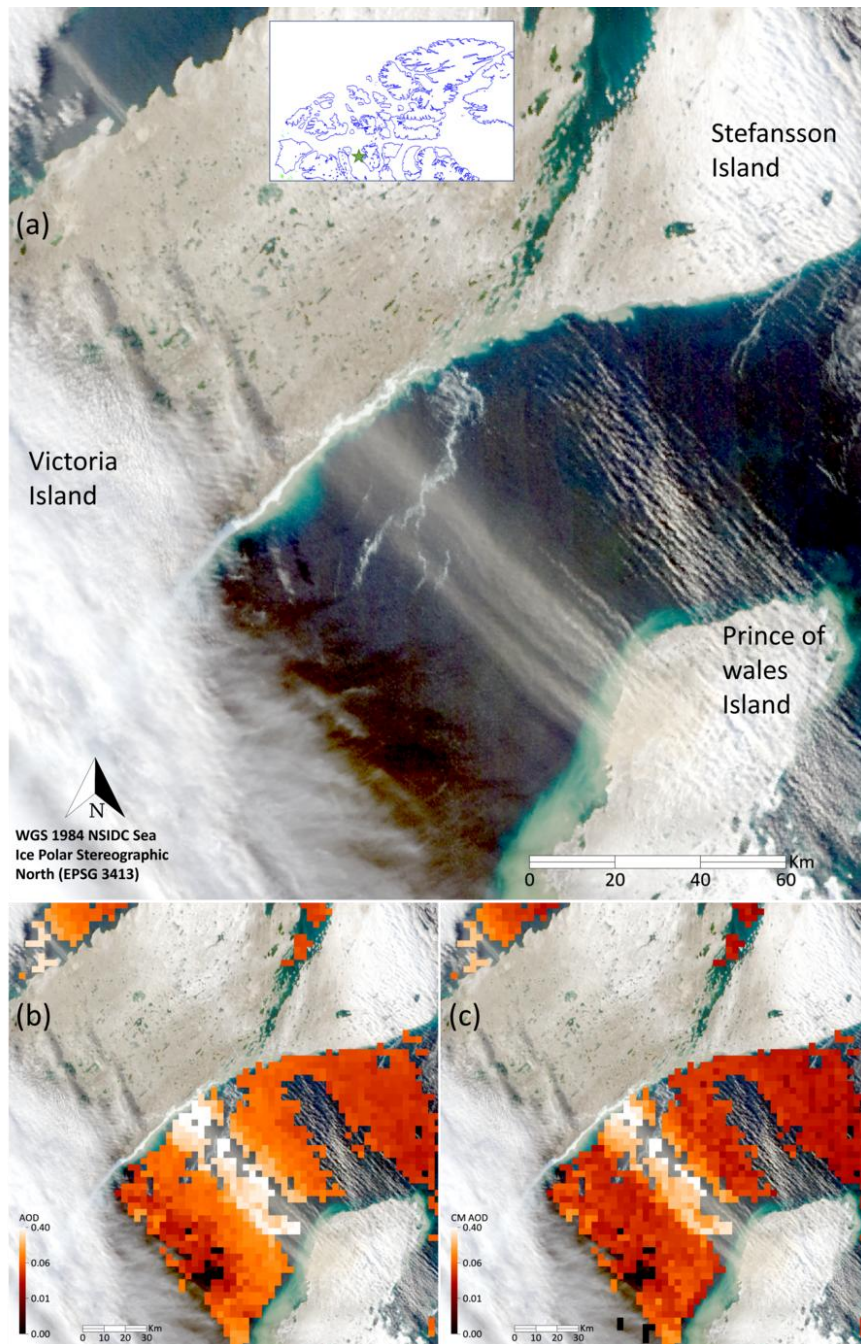
374

---

<sup>30</sup> Supplementary PowerPoint file “Satellite\_Analysis”

<sup>31</sup> We note that in general, neither the plume height or the plume speed sampling trajectories are subject to any objective sampling protocol and that the plume height (and plume speed) histograms generally represent significant departures from a normal distribution. While we report means and standard deviations of plume height and wind speed, they are meant to be order-of-magnitude height and height variability indicators for subjectively selected plume structures seen in the color imagery.

<sup>32</sup> An ECCC met station (WMO ID: 71017, coordinates  $73^{\circ}46'N$ ,  $105^{\circ}18'$ ) at 11 m elevation is located on Stefansson Island (see Fig. 6). We normalized the MISR plume speed to the plume speed at the elevation of the station by applying a standard wind gradient expression (see .e.g. Kaltschmitt et al., 2007) with an open-water wind shear (Hellman) exponent of 0.1:  $ws(h) = ws_{ref}(h/h_{ref})^a$ ,  $ws_{ref} = ws(h)(h/h_{ref})^{-a} = 75(298/11)^{-0.1} = 54$



375

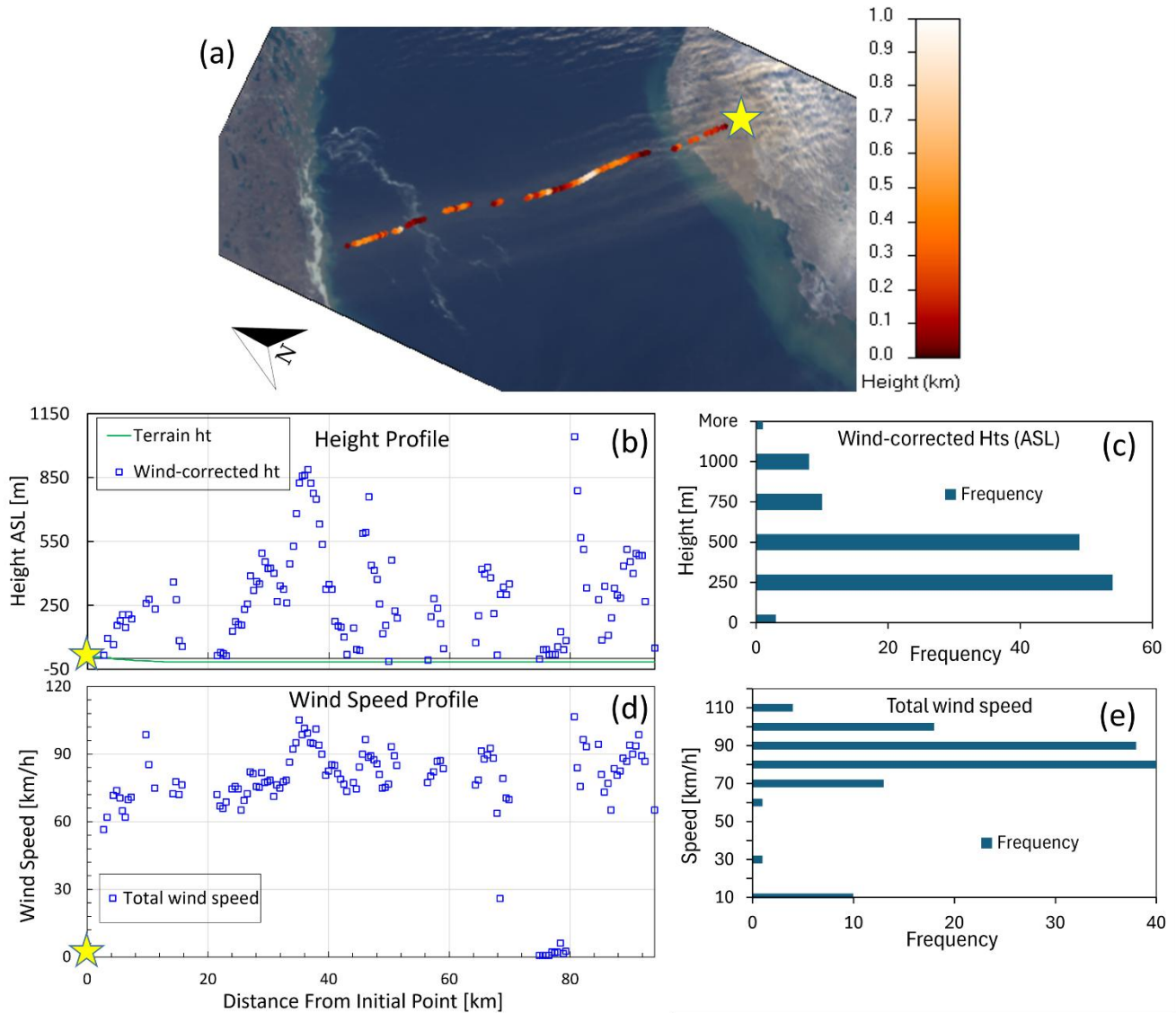
376

377

378

379

**Figure 6 – local dust event (over Prince of Wales Island and Victoria Island) captured on 26 September 2015. (a) MODIS Terra true-color image acquired at 19:10 UTC (b) AOD product, (c) CM AOD. Note that there appear to be distinct water plumes before and after the barren region on Prince of Wales Island (water plumes that were captured by the MODIS cloud OD product and are distinctly unique in the color image).**



381

382

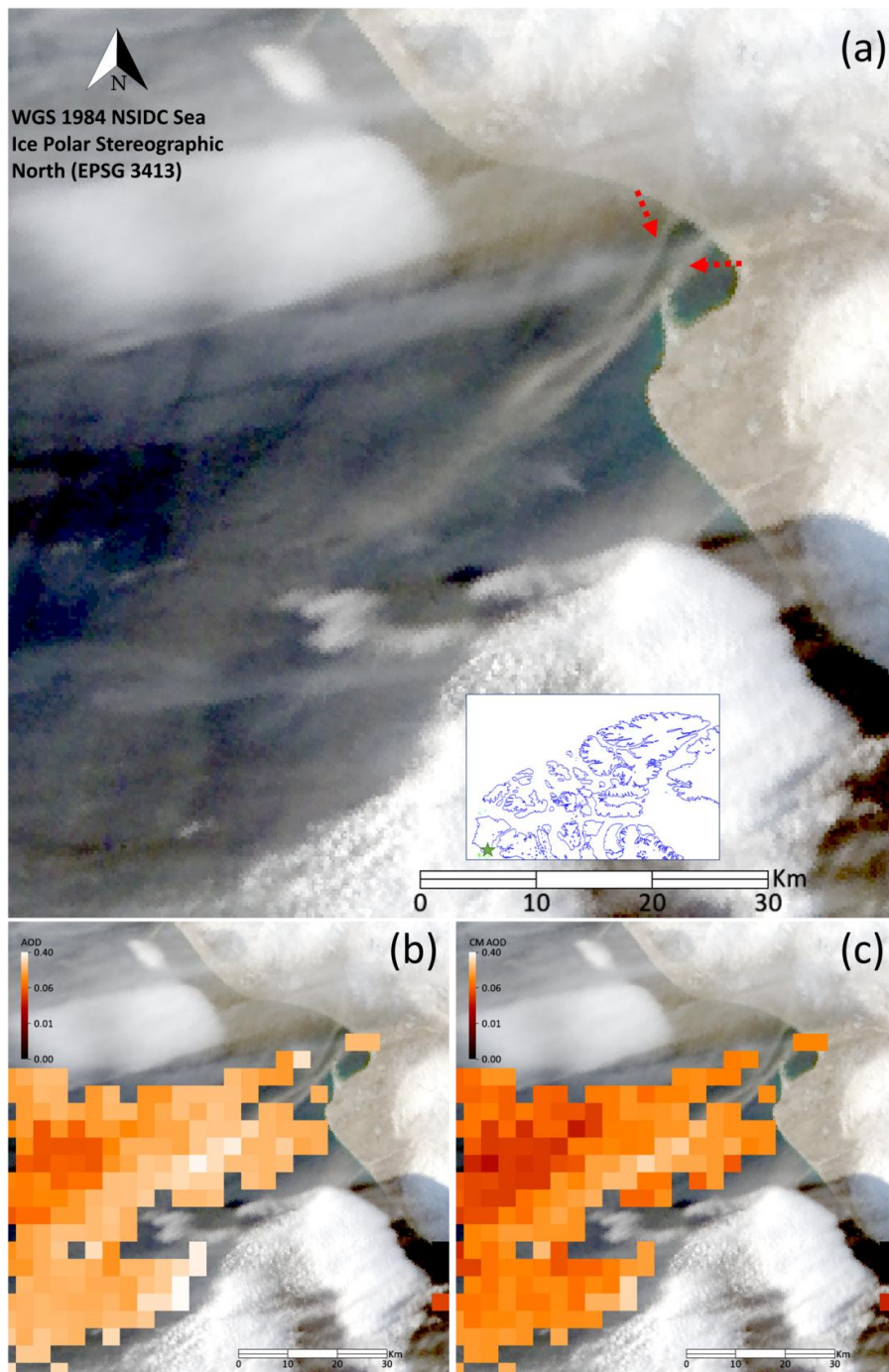
383 **Figure 7 – (a) MISR nadir (An camera) true color image acquired at 19:12 UTC (275 m resolution) with retrieved MISR plume**  
 384 **height values along a selected trajectory (the red-orange path that begins with a yellow star and whose color legend appears to the**  
 385 **right of the image) superimposed on the color image, (b) trajectory plume heights as a function of distance from the reference point**  
 386 **(yellow star) and (c) the histogram of those selected plume heights. The (d) and (e) graphs are the corresponding wind (plume) speed**  
 387 **trajectory values and histogram. We note that the MINX assumption of no vertical plume motion may reduce the plume height**  
 retrieval accuracy (Nelson et al., 2013).

### 388 4.2.3 Dust event in the southwest corner of the CAA

389 The red arrows of Fig. 8a delineate what we argue are a pair of local dust plumes emanating from largely vegetation-free areas  
390 on Banks Island (the southwest corner of the CAA) and flowing south over the Amundsen Gulf (MODIS-Terra color image  
391 acquired at 20:20 UTC on October 1, 2018). Some plume widths are sufficiently thin that the moderate resolution MODIS and  
392 MISR color imagery (as well as the coarser resolution of the MODIS 3 km AOD product) diffuses out much of the fine spatial  
393 detail. The AOD product and the derived CM AOD (Figures 8b and 8c) appear to capture the general individual plume patterns  
394 seen in the color imagery (and their apparent broadening into a single plume). The MODIS CM AOD values in the vicinity of  
395 those plumes range from  $\sim 0.03$  to  $0.26$  (while AOD values range from  $\sim 0.04$  to  $0.37$ ).

396 This was a complicated case with high altitude cirrus being (at least qualitatively) confused with the very low altitude dust  
397 plumes. The issue can, on a visual level, be resolved by deferring to animations of the multi-angle MISR views where the  
398 separation of the former from the latter (in terms of their apparent stereoscopic ground speed relative to the fixed ground scene)  
399 is evident (see that animation in Fig. S19). Figure S20 shows a sampling trajectory of the double dust plumes that are pointed  
400 to by the red arrows of Fig. 8a. The mean and standard deviation of the MISR plume height and wind (plume) speed histograms  
401 along this trajectory are respectively  $196 \pm 155$  and  $25 \pm 25$  km / h (the latter value belonging to a distinctly non-normal  
402 distribution).

403 The geographic details of the two thin dust plumes seen in the MODIS-Terra color image of Fig. 8a along with even weaker  
404 and thinner dust plumes elsewhere in the region are brought into rather striking relief in zooms of a high-resolution Sentinel-  
405 2 image. Figure S21 shows, what amounts to, apparent source information for five different plumes (including source  
406 information for one of the two thin dust plumes seen in the MODIS image). Those zoomed images give valuable, if indirect,  
407 contextual information on the source and dynamics of the plumes. One can, for all five cases, see a water to land dust plume  
408 continuity with the plume origins being either (a) very low altitude dust plumes over the land or (b) surface features of the  
409 sources.



410

411

412

**Figure 8 – (a) Local dust plumes emanating from Banks Island on October 1, 2018 (MODIS Terra true color image acquired at 20:20 UTC). Figures (b) and (c) show the MODIS Terra AOD and the derived CM AOD superimposed on the color image**

#### 413 **4.3.4 Dust plumes emanating from Ellef Ringnes Island (eastern part of the central CAA)**

414 The 20:10 UTC, September 13, 2014 MODIS-Terra true color image of Fig. 9a shows what appear to be local dust plumes  
415 emanating from dark brown regions of Meteorologist Peninsula<sup>33</sup> and flowing over the open-water region at the southern tip  
416 of that peninsula. Figures 9b and 9c show the MODIS AOD product and estimated CM AODs over a part of that open-water  
417 region: the spatial variation of those AODs and CM AODs are qualitatively coherent with the perceived spatial variations of  
418 the dust plumes in the true color image of Fig. 9a. Figure S23 shows zoomed-in details: one can observe that the thickest part  
419 of the plumes as seen on the color image and the largest CM AODs are aligned with the brownish regions (presumably sources)  
420 on Meteorologist Peninsula. CM AOD values in Fig. 8b and 8c range from  $\sim 0.05$  to  $0.47$  while the AOD values range from  $\sim$   
421  $0.11$  to  $0.50$ .

422 Figures S24 and S25 show a selected MISR trajectory case over the open water west of Meteorologist Peninsula (Fig. S22  
423 shows the [subjective] investigation that was carried out to determine the color image enhancement that best permitted one to  
424 appreciate how the trajectory was embedded in the dust plume<sup>34</sup>). The mean wind-corrected plume height is  $264 \pm 162$  m for  
425 the trajectory while the mean plume speed is  $38 \pm 14$  km / h. Normalizing the latter value to the height of the nearest met  
426 station<sup>35</sup> yields normalized wind speeds of  $32$  km / h. This is moderately lower than the 20:20 AUT met station value of  $51$  km  
427 / h and 1.7-times its climatologically (1996 – 2025) mean wind speed for the month of September ( $18.8 \pm 13.5$  km / h).

428 In the absence of a standard AOD product we developed an ad hoc AOD retrieval technique for the dirty brown snow/ice  
429 region between Meteorologist Peninsula and King Christian Island (see Fig. S26 and its caption for details on that ad hoc  
430 technique). The results of that retrieval showed a coarse degree of AOD continuity across the ice/snow to water interface<sup>36</sup>  
431 (see the blinking animation of Fig. S27). Evidence that the dirty brown area was (at least in part) a dust plume and not deposited  
432 dust is provided by a MISR height profile showing plume heights varying between  $0$  to  $\sim 500$  m (Fig. S28). The corresponding  
433 plume speeds of  $42 \pm 20$  km / h are moderately greater than the plume speeds over water.

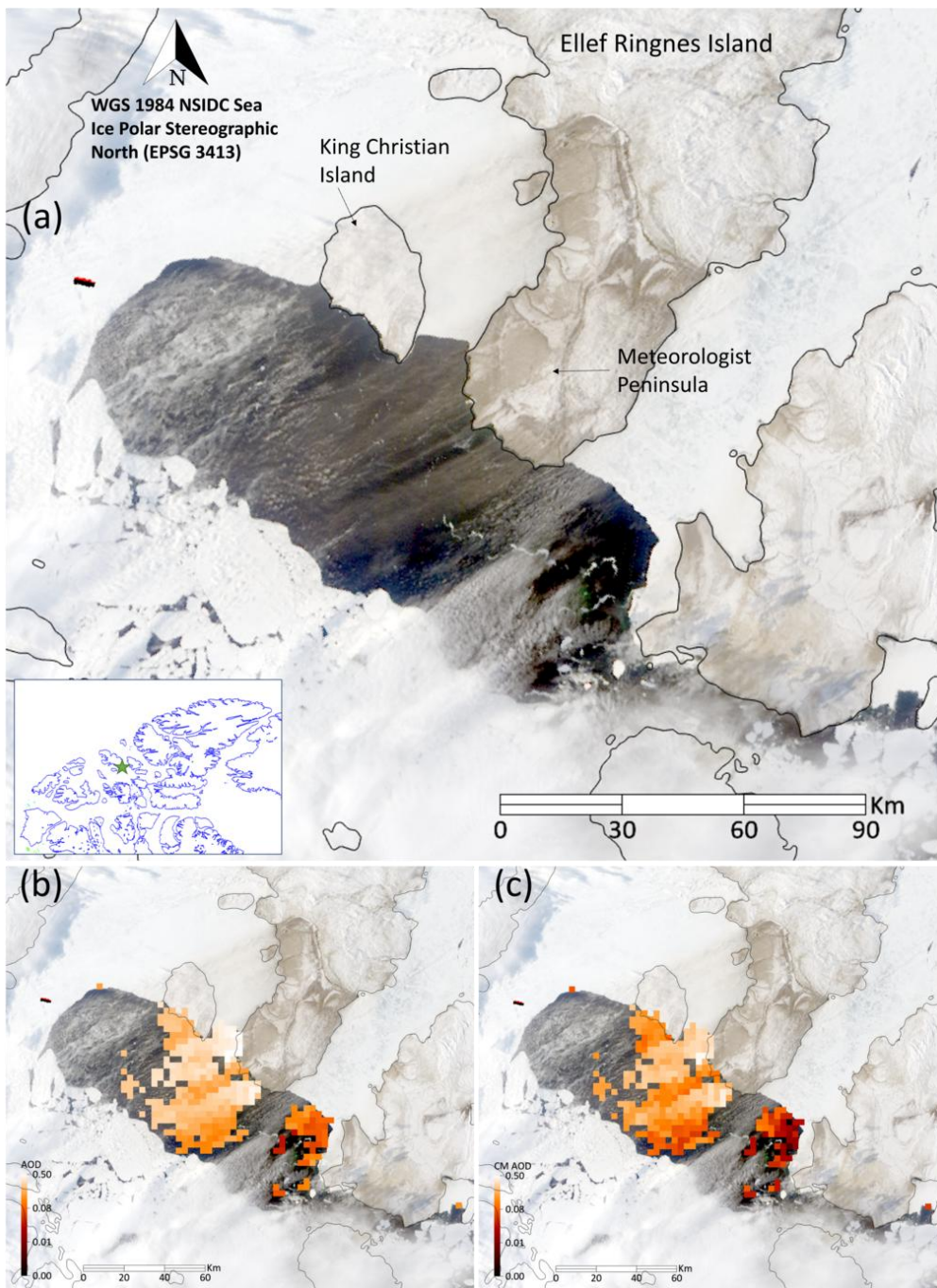
---

<sup>33</sup> Meteorologist Peninsula is located at the extreme south of Ellef Ringnes Island (again, see Fig. 9a)

<sup>34</sup> Figure S24 shows the MISR camera animation where one can more readily appreciate the positions and stereoscope movement of higher altitude clouds.

<sup>35</sup> The 58 m ECCC met station of “ISACHSEN (AUT)” in the north of Ellef Ringnes Island ( $78^{\circ}47'N$ ,  $103^{\circ}33'W$ ). The normalization approximation for wind-shear (wind gradient) effects was carried out as per Section 4.2.2 above.

<sup>36</sup> there is no CM AOD option for the snow/ice retrievals since we have no CMF estimate for those retrievals



434

435

436

437

438

Figure 9 – MODIS-Terra true color imagery (logarithmic enhancement) acquired at 20:10 UTC over Ellef Ringnes Island on Sept. 13, 2014 (a) local dust plumes over the water emanating from Meteorologist Peninsula on Ellef Ringnes Island. Figures (b) and (c) show the MODIS Terra AOD and derived CM AOD superimposed on the color image (see Fig. S23 in the supplementary PowerPoint file “Satellite\_Analysis” for a full resolution comparison of the AODs and the color image).

#### 439 **4.4 Surface plume deposition / snow melt; snow/ice reflectance changes as optical precursors of dust plumes**

440 The RS of airborne Arctic dust can be advantageously complemented by the RS of reflectance changes (darkening) induced  
441 by the deposition of airborne dust on snow or ice and/or reduced reflectance incited by premature snow melt due to dust  
442 deposition. Woo et al. (1991) noted that the presence of snow-melt zones over the Fosheim Peninsula on Ellesmere Island  
443 corresponded to dark spots in early AVHRR imagery. Ranjbar et al. (2021) found roughly the same dark patterns in true color  
444 MODIS imagery and showed visual evidence of deposition of dust on snow (or underlying soil subsequent to snow melt) in a  
445 mosaic of true color MODIS imagery acquired over the whole of Ellesmere Island.

446 O'Neill et al. (2025) argued that the combination of persistent day to day dark zones in MODIS imagery and the lack of  
447 movement of those features in MISR multi-angle imagery was indicative of local-dust surface deposition in the case of Prince  
448 Patrick Island and neighbouring Eglinton Island (west central CAA). We found what appeared to be a more dynamic MISR  
449 example of deposited dust across the Strand Bay region of Axel Heiberg Island over a three-day period (see Fig. S29). Figure  
450 S30a shows the MISR height profile of a June 8, 2007, airborne dust plume and the position of its sampling trajectory on the  
451 associated MISR (nadir) image<sup>37</sup>. The plume profile of Fig. S30b (acquired two days later) shows what appears to be near-  
452 zero heights in a region where the color image indicates a much darker pattern than that of Fig. S30a<sup>38</sup> (accompanied by a rise  
453 in plume height near the northern shore of Strand Bay). We would suggest that the darkest region of Strand Bay in the color  
454 image is likely a dynamic example of the process of dust deposition. In this particular case, the source of the (very dark) dust  
455 is likely the volcanic deposits known to characterize much of the Strand Fjord Formation (Williamson & MacRae, 2015).

#### 456 **5 Conclusions**

457 Ground-based RS and microphysical measurements acquired at the PEARL complex in Eureka were employed to investigate  
458 the potential for satellite-based and ground-based RS of local dust plumes. This analysis supported and / or complemented  
459 explicit examples of satellite-based RS of local dust events near Eureka and across the CAA.

460 Ground-based RS validation results were obtained (in terms of the identification and characterization of local dust events) with  
461 significant correlations in 2007 data between the 0PAL (ground-based) CM AOD and the lidar-derived CM AOD (and the  
462 lack of correlation with the 615 m above-plume CM AOD at the Ridge Lab). The late-summer correlations (Aug, 21, 2018  
463 data) between APS CM particle-volume concentration ( $v_c$ ) measurements and 0PAL CM AODs along with the similarity  
464 between the APS and AERONET PVSDs suggest a significant 1.3 – 1.5  $\mu\text{m}$  radius peak that was due to local dust of weak  
465 CM AOD ( $\leq 0.01$ ). This is notable given the near-1.3  $\mu\text{m}$  radius AERONET peaks reported by SDN for a springtime (May)  
466 measurement campaign at the KLRS site in the Yukon (a peak which they ascribed to springtime Asian dust).

---

<sup>37</sup> The MISR image shows numerous dust plumes which appear to be associated with dark sources on the southern shore of Strand Bay.

<sup>38</sup> Note that the MISR times of S30a and S30b images are nearly identical (solar illumination conditions are nearly identical)

467 Indirect linkages were made between the surface RS and microphysical data and available satellite on the Aug. 21, 2018, RS  
468 imagery acquired in the neighbourhood of Eureka: we argued that a weak but detectable plume over Eureka Sound (MODIS  
469 AODs  $\lesssim 0.1$ ) might be related to the very weak CM AODs measured by the OPAL CIMEL (values of  $\lesssim 0.01$  that are typically  
470 undetectable by satellite RS). More direct linkages were made with OPAL wind speed ( $ws$ ) measurements and regional  $ws$   
471 (reanalysis) values. It was argued that above normal OPAL  $ws$  values and above normal regional  $ws$  values coupled with co-  
472 incident increases in CM AOD and  $v_c(0)$  measurements at OPAL were evidence of a region-wide wind event that caused local  
473 and regional dust disturbances.

474 A pan-CAA analysis using the multi-dimensional information available from MODIS color imagery and its AOD products,  
475 MISR multi-camera, stereoscopic imagery, MINX (MISR) estimates of plume height and speed and high spatial resolution  
476 Sentinel-2 imagery supported by measured and /or regional  $ws$  products indicated that local dust plumes of relatively weak to  
477 strong optical thickness (CM AOD ranging from  $\sim 0.02$  to  $0.60$ ) at generally sub-km plume heights could be detected from  
478 available satellite products. A sampling of key parameters for all plume events is given in Table 1. In what follows we give a  
479 summary of those pan-CAA conclusions.

480 A Sept. 20, 2020 plume event north of the Fosheim Peninsula showed evidence of plume dynamics that were roughly coherent  
481 with CARRA wind vector patterns and whose spatial variation (colour image pattern) was similar to the spatial pattern of the  
482 derived CM AODs. The MINX (MISR) plume height and speed of (September 26, 2015) dust plumes flowing from Prince of  
483 Wales Island to Victoria Island (southern part of the CAA) were  $300 \pm 230$  m ASL and  $75 \pm 24$  km / h (while MODIS CM  
484 AOD values ranged from 0.02 to 0.56). The  $54$  km / h value<sup>39</sup> for that event is abnormally large (3 times the climatological  
485 mean for September).

486 Information from MISR, MODIS and Sentinel-2 color imagery was employed to identify dust plumes (partially obscured by  
487 higher altitude clouds) emanating from local dust sources on Banks Island (southwest corner of the CAA) in October of 2018.  
488 The MODIS CM AOD values, for the Banks Island satellite events varied from to 0.03 to 0.26 and visually corresponded to  
489 what appeared to be dust plumes in the MODIS color imagery (supported by the stereoscopically determined distinctions  
490 between clouds and low-level plumes provided by the MISR imagery). The Sentinel-2 color imagery provided a unique high-  
491 spatial-resolution perspective that enabled the distinction of the land to water continuity of a few local dust plumes. A  
492 moderately strong dust event emanating from Ellef Ringnes Island in September of 2014 was characterized by CM AODs  
493 between  $\sim 0.05$  to  $0.47$ , mean plume heights of  $\lesssim 300$  m and mean plume speed (normalized to the elevation of the nearby met  
494 station) of  $32 \pm 12$  km / h (1.7 times the climatological mean of the nearby [Stefansson Island] met station for the month of  
495 September).

496 We employed MINX (MISR) color imagery and plume height retrievals to argue that June, 2007 Strand Bay (Axel Heiberg  
497 Island) MISR images of a dirty snow / ice surface showed both a plume above the surface and what appeared to be plume

---

<sup>39</sup> the measured value normalized to the height of the nearby met station

498 deposition (zero altitude plume retrievals) over the surface two days later (with a much darker reflectance). This appears to be  
 499 a rather rare example of a commonly cited phenomenon (dust plume deposition effects). The RS identification of dust  
 500 deposition events on snow presents a unique opportunity for monitoring the attendant changes in snow reflectance (and  
 501 premature snow melt events) across different Arctic regions.

502 In summary, a series of dust events involving distinct, narrow plumes, at least partly over dark water, downwind of likely dust  
 503 sources and typically under contemporaneous high-wind conditions were identified. The use of the MODIS and/or MISR  
 504 and/or Sentinel-2 imagery (coupled with geographical and meteorological information) for identifying and characterizing local  
 505 dust plumes requires careful analysis: however, the benefits often include a synergistic characterization of plume properties  
 506 that significantly exceed what can be extracted from a single sensor. The specialized advantages of each of these RS sensors  
 507 should be understood before undertaking such an approach: our greatest strategic realization, for example, was that, in spite of  
 508 the obvious advantages of the CALIOP lidar in characterizing dust plume properties, the MISR imager has a much greater  
 509 chance of detecting a spatially constrained plume (CALIOP being limited to a single orbit line rather than broad, along-track,  
 510 MISR images).

511

512 **Table 1: Summary of CAA dust events captured using satellite-based RS. See footnote 37 concerning the reporting of means and**  
 513 **standard deviations for plume height and plume speed.**

Source location (Island)	Date and time (dd/mm/yyyy, hh:mm) [UTC]	Approximate coordinates of plume source (lat, lon) [deg]	AOD (min, max)	CM AOD (min, max)	Visible plume length [km]	plume height (ASL) [m]	plume speed [km/h]
<b>Axel Heiberg Island</b>	08/09/2020, 15:20	(80.05, -87.55)	(0.06, 0.42)	(0.02, 0.31)	60	NA	NA
<b>Prince of Wales Island</b>	26/09/2015, 19:10	(72.65, -102.36)	(0.06, 0.73)	(0.02, 0.56)	110	300 ± 230	75 ± 24
<b>Banks Island</b>	01/10/2018, 20:20	(71.46, -121.74)	(0.04, 0.37)	(0.03, 0.26)	50	196 ± 155	25 ± 25
<b>Ellef Ringnes Island</b>	13/09/2014, 20:10	(77.83, -99.50)	(0.11, 0.50)	(0.05, 0.47)	60	264 ± 162	38 ± 14
<b>Axel Heiberg Island (Strand Bay)</b>	08/06/2007, 19:59	(79, -93.25)	NA	NA	20	165 ± 99	1.6 ± 1.2
<b>Axel Heiberg Island (Strand Bay)</b>	10/06/2007, 19:47	(79, -93.25)	NA	NA	20	40 ± 40	2 ± 2

514

## Appendix A

### A1: Comparing CIMEL- and AHSRL-derived AODs

#### A1.1: CIMEL-based FM and CM attribution

Given the unique arrangement of the two CIMELs at Eureka, one near the OPAL site (superscript “O” and one at the higher altitude PEARL (Ridge lab) site (“P” subscript), the (500 nm) FM, CM and total AODs of the layer between the two sites (assuming optical homogeneity above P between the two different lines of site) are,

$$\Delta\tau_f = \tau_f^O - \tau_f^P \quad (A1a)$$

$$\Delta\tau_c = \tau_c^O - \tau_c^P \quad (A1b)$$

$$\text{and } \Delta\tau_a = \tau_a^O - \tau_a^P = \tau_f^O + \tau_c^O - (\tau_f^P + \tau_c^P) = \Delta\tau_f + \Delta\tau_c \quad (A1c)$$

#### A1.2: Temporal resampling considerations for the two CIMELs and the lidar

1.  $\tau_c^{l,O}$  represents  $\tau_c^l$  resampled to  $\tau_c^O$  times while we use  $N^{l,O}$  to describe the number of resampled points. For the sake of keeping the nomenclature as simple as possible, we dropped the “O” superscript from  $\tau_c^{l,O}$  (i. e. there is only one lidar).
2.  $\tau_c^{p,O}$  represents  $\tau_c^p$  resampled to  $\tau_c^O$  times<sup>40</sup> while using  $N^{p,O}$  to represent the number of resampled points.  $N^{p,O} \neq N^{l,O}$  if, for example, the PEARL measurements are limited in temporal extent relative to the OPAL temporal extent.
3. Accordingly,  $\Delta\tau_c$  is more precisely defined as  $\tau_c^O - \tau_c^{p,O}$ .

We employ  $N^O$  to represent the common lidar and PEARL resample points ( $N^O = N^{l,O} = N^{p,O}$ ).

The resampling applied to estimate  $\tau_c^l$  or  $\tau_c^{p,O}$  was respectively nearest neighbour<sup>41</sup> and linear interpolation<sup>42</sup>

#### A2: FM and CM attributions for the AHSRL lidar

If the FM and CM PDR (particle depolarization ratio<sup>43</sup>) candidates are defined by holistic FM and CM PDR distributions (whose size-averaged PDRs are  $\delta_f$  and  $\delta_c$ ) then the optically weighted average VDR can be written as;

---

<sup>40</sup> but  $\tau_c^p$  is shown in the PowerPoint profiles

<sup>41</sup> the value of  $\tau_c^l$  at the nominal  $\tau_c^l$  time contained within a particular OPAL (one-minute) time bin (where the general AERONET sampling frequency is every 3 minutes: see Giles et al., 2019 for details on CIMEL sampling),

<sup>42</sup> between the two  $\tau_c^p$  values at the two nominal PEARL times on either side of a particular  $\tau_c^O$  time

<sup>43</sup> PDR is a common (intensive-parameter) label for that is typically (if rather simplistically) associated with a given type of atmospheric particle. See, for example, Liu et al. (2013)

537 
$$VDR = \frac{\delta_f \tau_{\beta,f} + \delta_c \tau_{\beta,c}}{\tau_{\beta,f} + \tau_{\beta,c}} \quad (A2a)^{44}$$

538 
$$= \delta_f (1 - \eta_{\beta,c}) + \delta_c \eta_{\beta,c} \quad (A2b)$$

539 
$$= \delta_f \eta_{\beta,f} + \delta_c (1 - \eta_{\beta,f}) \quad (A2c)$$

540 where we define

541 
$$\eta_{\beta,c} = \frac{\tau_{\beta,c}}{\tau_{\beta,c} + \tau_{\beta,f}} \text{ and } \eta_{\beta,f} = \frac{\tau_{\beta,f}}{\tau_{\beta,c} + \tau_{\beta,f}} = (1 - \eta_{\beta,c}) \quad (A2d)$$

542 As we will argue below, the lidar optical depths ( $\tau_c^l$  and  $\tau_f^l$  in the main text<sup>45</sup>) can provide reasonable estimates of  $\tau_c$  and  $\tau_f$   
 543 for a strategic choice of  $\delta_{thr}$ . If the FM and CM PDRs are defined in a binary fashion by a  $\delta_{thr}$  threshold then those PDRs  
 544 can be written,

545 
$$\delta_f' = \langle VDR^{\delta \leq \delta_{thr}} \rangle \quad (A3a)$$

546 
$$\delta_c' = \langle VDR^{\delta > \delta_{thr}} \rangle \quad (A3b)$$

547 The “ $\langle VDR \rangle$ ” symbolism represents some weighted or unweighted VDR mean in altitude (or in altitude as well as time) where  
 548 the  $\delta_{thr}$  criterion is applied to every single lidar pixel. Equation (A2) represents a tool for seeking out information about the  
 549 PDRs of holistic depictions of FM and CM components. One must be wary of the opto-physical differences between  $\delta_f$  and  
 550  $\delta_c$  versus  $\delta_f'$  and  $\delta_c'$  respectively<sup>46</sup> and their link with the measured  $VDR$  (or averages of measured VDRs). The two  
 551 formulations can be investigated by varying  $\delta_{thr}$  until some optimal solution is obtained for any given event. Part of the process  
 552 is the recognition that  $\delta_f$  is known (empirically and theoretically) to be small ( $\lesssim$  a few %; see Fig. A1 for example) while  $\delta_c$   
 553 of dust particles generally increases with increasing  $\delta_{thr}$  in the range where dust-particle population is significant<sup>47</sup>. We  
 554 suppose that the PDR of other particulate species (clouds, for example) are easily separable from our FM and CM aerosol  
 555 species.

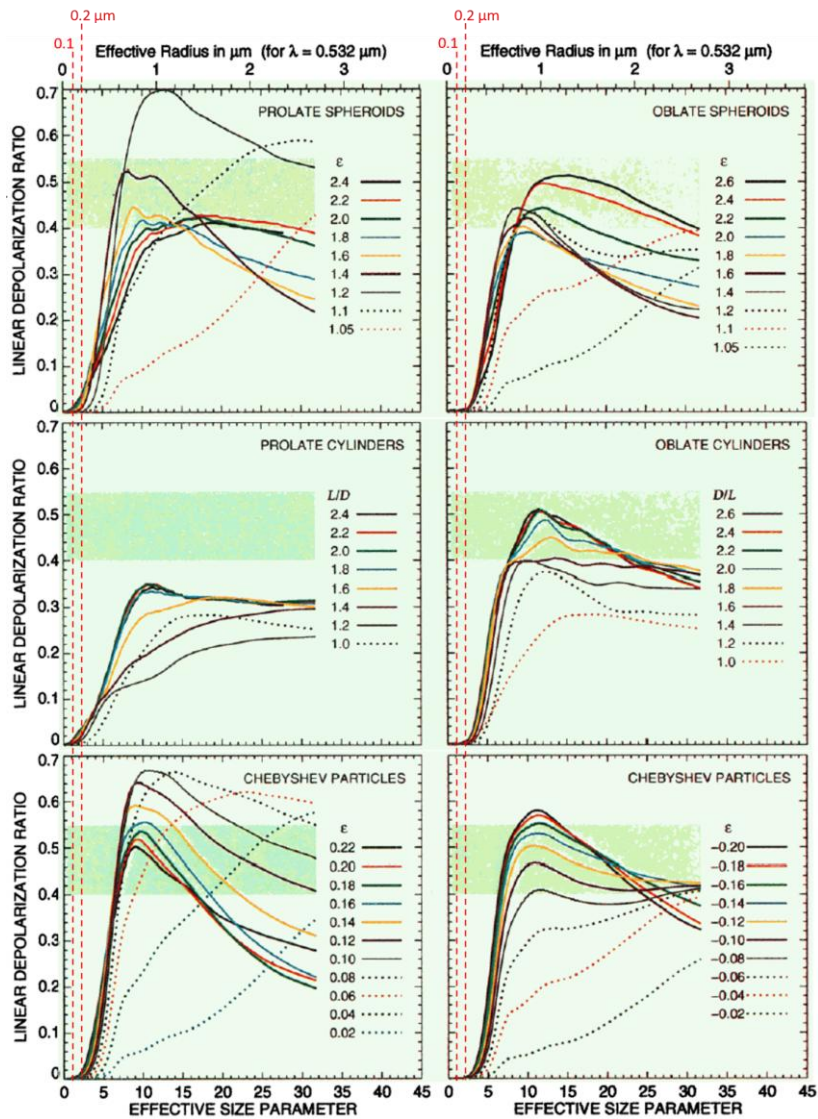
---

<sup>44</sup> Where FM and CM (lidar profile) pixels can be defined, respectively by  $\delta \leq \delta_{thr}$  &  $\delta > \delta_{thr}$  if there is a  $\delta_{thr}$  saddle between the PDRs

<sup>45</sup> where  $\tau_c^l = S_c \tau_{\beta,c}$  and  $\tau_f^l = S_f \tau_{\beta,f}$  ( $S_c$  and  $S_f$  being their respective lidar ratios)

<sup>46</sup> Equation (A2) represents a continuously varying function of  $\eta_c$  or  $\eta_f$  while equation A3 is a step function of  $\delta_{thr}$  (stepping from  $\delta_{thr}$ -  
 dependent values of  $\langle VDR \rangle$  for  $\delta \leq \delta_{thr}$  to  $\delta_{thr}$ -dependent values of  $\langle VDR \rangle$  for  $\delta > \delta_{thr}$ )

<sup>47</sup> Where the particle volume sized distribution is significant: see, e.g., Mamouri & Ansmann, 2014 (MA)



556

557

558

559

560

**Figure A1** – Computed variation of the 532 nm DR as a function of effective radius (top horizontal scale) and various assumed ice particle shapes (Fig. 1 of Mischenko & Sasson, 1998). Optically significant, column-integrated FM particles are largely contained within a radius range of 0.1 to 0.2  $\mu\text{m}$  (indicated by the red-dotted vertical lines which we appended to the original figure). This demonstrates that the PDR of FM particles is  $\approx$  a few % for all particle shapes considered by the authors.

561

### A3: The need for vertically-averaged VDR weighting

562

563

564

AHSRL  $\beta$  and VDR profiles (along with derived values of lidar, OPAL and PEARL CM AODs) for the 7 Eureka dust events that we investigated can be observed in the supplementary PowerPoint file “AHSRL\_CIMEL\_event\_profiles”. The VDR values ranged from small-amplitude negative to positive values to large-amplitude negative and positive outliers (see Section

565 A3.1 for a detailed discussion of how we processed that data). Dörnbrack et al. (2010) reported on airborne lidar observations  
566 and characterization of local dust events over Svalbard in May of 2004. Their results included dust plumes whose VDRs ranged  
567 from quite small ( $\lesssim 5\%$ ) to values larger than 10% inside the plumes to maximum values of  $\lesssim 30\%$  very close to the surface.  
568 In the context of the discussion presented in Section A2, VDRs of local dust profiles can achieve (extreme FM to CM) values  
569  $\sim 15 - 40\%$ <sup>48</sup>. MA report that their holistic FM component<sup>49</sup> produces PDRs ( $\sim 5\%$ <sup>50</sup>) while also demonstrating that their sub-  
570  $\mu\text{m}$  FM dust tail<sup>51</sup> can induce a significant VDR increase relative to the holistic FM component<sup>52</sup> and that super- $\mu\text{m}$  particles  
571 can induce even larger VDRs. See Figures 3a and 3b above for empirical examples showing a super- $\mu\text{m}$  CM peak radius at  
572 our OPAL site (after the advent of the stronger dust event at 20:30 UTC).

### 573 **A3.1: VDR weighting options.**

574 VDR profile averages ( $\langle VDR \rangle$ ) between 82 and 615 m<sup>53</sup> were found, in the initial processing run, to be systematically too  
575 large<sup>54</sup>. This was suspected to be due to the initial choice of not including negative VDR pixels in any given VDR profile  
576 average<sup>55</sup>. Indeed, Fig A2 shows that the simple removal of negative VDR pixels (blue-colored circles) produced  $\langle VDR \rangle$   
577 estimates that were systematically greater than the two more statistically justifiable methods<sup>56</sup>. Two alternate methods were  
578 investigated to mitigate the impacts of removing negative VDRs :

- 579 ○ The 1<sup>st</sup> method (green circles) employs no weighting but does not exclude negative VDRs.

---

<sup>48</sup> See, e.g. MA who argue that their FM and CM dust PDRs [ $“\delta_{df}”$  and  $“\delta_{dc}”$  respectively] of 16 and 39% respectively can generate near-source (Sahara) VDR ( $\delta$ ) values of  $\sim 31 \pm 3\%$  (the values of Freudenthaler et al., 2009 and Grob et al., 2011 as cited in MA).

<sup>49</sup> e.g., the complete (and ubiquitous) FM AERONET-inversion component between  $\sim 0.05 - 0.2 \mu\text{m}$  (radius) seen in their Fig. 4.

<sup>50</sup> for what they call “non-dust” particles but whose distinctive feature is arguably the limitation to a holistic FM component. See also, for example, the precipitous drop in simulated  $\delta$  values of ice particles (to magnitudes  $< 5\%$ ) for (ice) between the specific cases of 0.05 and  $0.2 \mu\text{m}$  radius (effective size parameter between 0.6 and 2.4) in Fig. A1.

<sup>51</sup> the tail of what might be called a holistic CM component between  $\sim 0.2$  to  $10 \mu\text{m}$  radius as seen in their Fig. 4

<sup>52</sup> MA’s AERONET PSD shows a not insignificant (sub- $\mu\text{m}$ ) FM tail of that CM component. It is this tail that surely drives their FM ( $“\delta_{df}”$ ) estimate of 16 %.

<sup>53</sup> the difference in elevation between OPAL and PEARL (except that the 82.5 m is above the OPAL elevation of 5 m). The statistics start at 82.5 m because the VDR below 82.5 m was judged to be too noisy.

<sup>54</sup> too many values well above the typical VDR range for CM dust (see, for example, Fig. 1 of Tian et al., 2020).

<sup>55</sup> While retaining the rest of the (positive) VDR pixels in the given profile

<sup>56</sup> Simply put the exclusion of the negative values acted to increase the  $\langle VDR \rangle$  values. This exclusion is debatable given that those negative values could well have a physical sense (they are likely associated with system constants whose range of variability could facilitate the production of negative VDR values for a fraction of the VDRs).

- The 2<sup>nd</sup> method includes a weighted mean of all VDRs in any given profile ( $\langle VDR \rangle_\omega = \sum \omega VDR / \sum \omega$  where  $\omega = 1/RE^2$  for each profile pixel<sup>57</sup>. This takes all VDRs into consideration (does not suffer from the negative-VDR limitations) and seems to produce more realistic  $\langle VDR \rangle$  values than the 1<sup>st</sup> method (values whose  $\langle VDR \rangle$  range extends less into (both) the negative region and the positive region. Averaging in time (averaging over the event using an optical weighting factor of  $\tau_\beta$ ) would then be written as;

$$\langle \langle VDR \rangle_\omega \rangle_{\tau_\beta} = \sum \langle VDR \rangle_\omega \tau_\beta / \sum \tau_\beta \quad (A4)$$

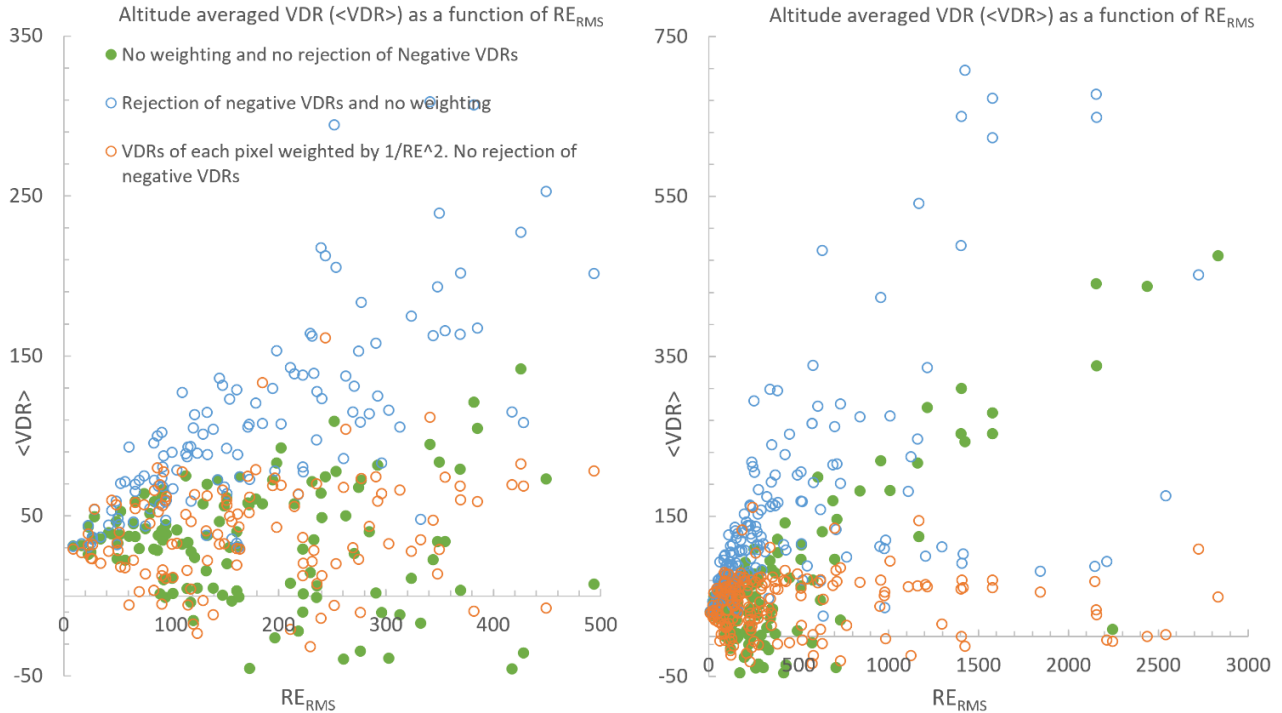
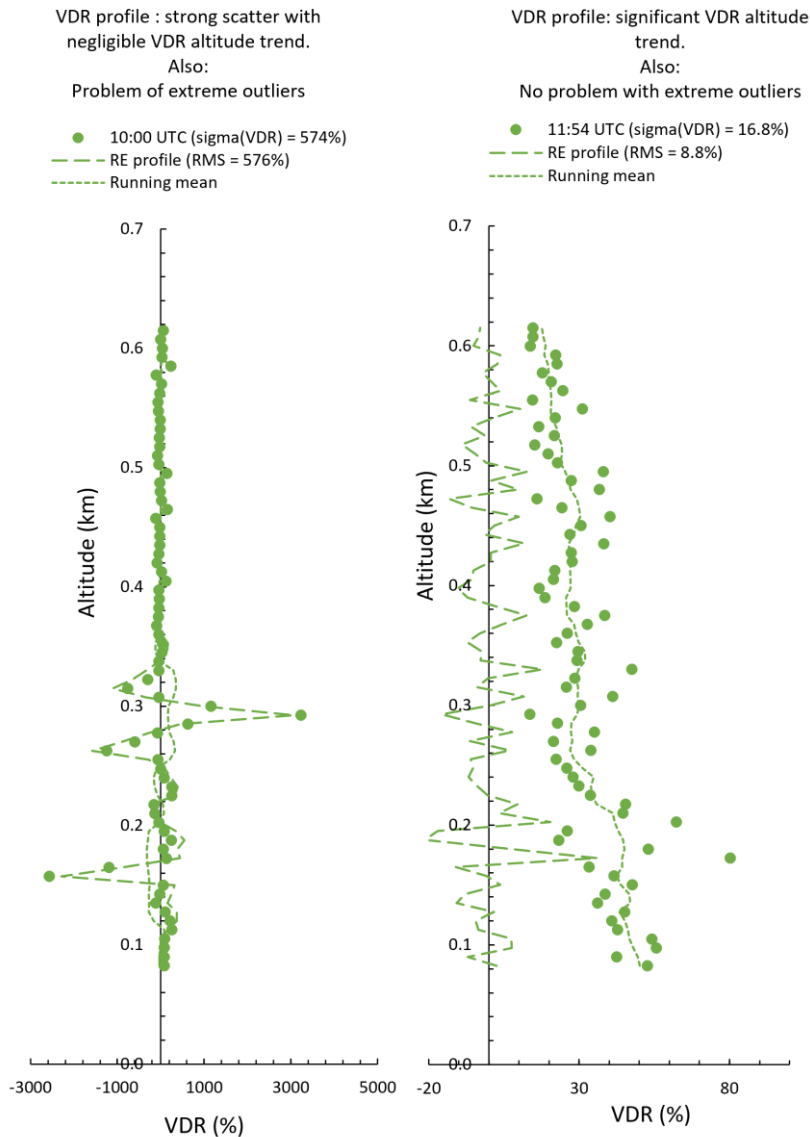


**Figure A2 – Altitude-averaged VDRs vs RMS residual errors ( $RE_{RMS}$ ) for the July 23, 2007 dust event (the LH graph is a zoom of the RH graph). According to our notation, the orange-colored weighted averages should be labelled  $\langle VDR \rangle_\omega$ . These statistics were computed for the lidar altitude range from 82 to 615 m.**

<sup>57</sup> The “ $RE_{RMS}$ ” of the x axis in Fig. A2 represents the RMS residual error of the individual residual of any lidar pixel in any given vertical profile (the “individual residual” being the difference between a given VDR value at a given altitude and its running average; see the example for two representative lidar profiles in Fig. A3 below). This RE parameter enables an estimation of the noise magnitude by eliminating the systematic trend of the natural VDR variation. The inverse square weighting approach was inspired by standard texts on linear regression analysis (see, for example, Section 3.5 of Barford, 1967)



590

591

592

**Figure A3 – Two representative lidar profiles (solid-shaded circles), their running mean (dotted curve) and their residual error (RE) difference (dashed curve).**

593

**A3.2: VDR weighting: profile-level impacts and resulting event-averaged statistics.**

594

595

The impact of the  $\omega$  weighting discussed in the previous sections is seen in Figures S1b to S7b<sup>58</sup>. In a nutshell the weighting significantly reduced the intra-profile standard deviations for all events (the bottom graphics of Figures S1b to S7b). We

<sup>58</sup> Supplementary PowerPoint file “AHSRL\_CIMEL\_event\_profiles”

596 would also argue that the event-wide average of the intra-profile standard deviation is the best candidate to describe the event-  
 597 wide precision (noise) of our VDR estimates (see the Fig. S8 caption for details). On the other hand, the weighting introduced  
 598 a significant amount of VDR variance in 2 events where very little variance existed prior to the weighting process (Events 1  
 599 and 6 of Figures S1b and S6b)<sup>59</sup>. The Event 1 and 6 standard deviations of intra-profile, event-level statistics that are  
 600 summarized in the table of Fig. S8 are accordingly to be treated with caution. Indeed, the table shows explicitly that weighting  
 601 did dramatically reduce the intra-profile standard deviations of all events excluding Events 1 and 6. We accordingly use the  
 602 intra-profile statistics in the following section on the derivation of the PDRs for each event.

### 603 **A3.3: Estimation of the event-averaged CM PDR**

604 Figure A4 shows the event-averaged VDR and  $\tau_\beta$  values for both the FM and CM components as a function of  $\delta_{thr}$  (equation  
 605 A3 above<sup>60</sup>). The CM event averages are rather insensitive to small values of  $\delta_{thr}$  (arguably because the weak PDR of the  
 606 FM component and perhaps the weak DR of the sub- $\mu\text{m}$  tail of the holistic CM PDR have little impact at small values of  
 607  $\delta_{thr}$ ). They only begin to rise when, we would argue, the sub- $\mu\text{m}$  tail begins to play a more significant optical role (the larger  
 608 DR of the sub- $\mu\text{m}$  tail incites the beginning of a positive slope that starts to rise at  $\delta_{thr}$  values ranging from 5 to 15%. A stable  
 609 estimate of the dust PDR would occur at any value before the rises begin, say at  $\delta_{thr} \sim 5\%$

610 That 5% value was chosen to populate the event-dependent 532 nm PDR values of Table A1. Two of the Table A1 values  
 611 are beyond the (780 nm) VDR upper limit for CM dust found, for example, in Fig. 1 of Tian et 2020 (their upper limit was  $\sim$   
 612 50% for dust particles ranging in radius from  $\sim 1$  to  $5 \mu\text{m}$ <sup>61</sup>). On the other hand, all the Table A1 PDR values are largely  
 613 contained within the 532 nm lidar ratio spread of “giant” near-source Saharan dust particles reported by Esselborn et al.  
 614 (2009): their Fig. 9 lidar ratios vary between 40 and 60 sr for dust particles of volume median radii ranging from 4 to  $15 \mu\text{m}$   
 615 (a spread that encompasses the  $7 \mu\text{m}$  radius AERONET inversion dust peak that we report above in Fig. 3a). It should be  
 616 emphasized that choices such as the (“ $\omega$ ”) weighting scheme and the optimal  $\delta_{thr}$  value contain a level of subjective  
 617 variability (in terms of, for example, the strengths of the weights applied). These factors and other sources of variability  
 618 produce uncertainties that we estimate as being  $\sim \pm$  the “ $\sigma(\text{PDR})$ ” values of Table A1.

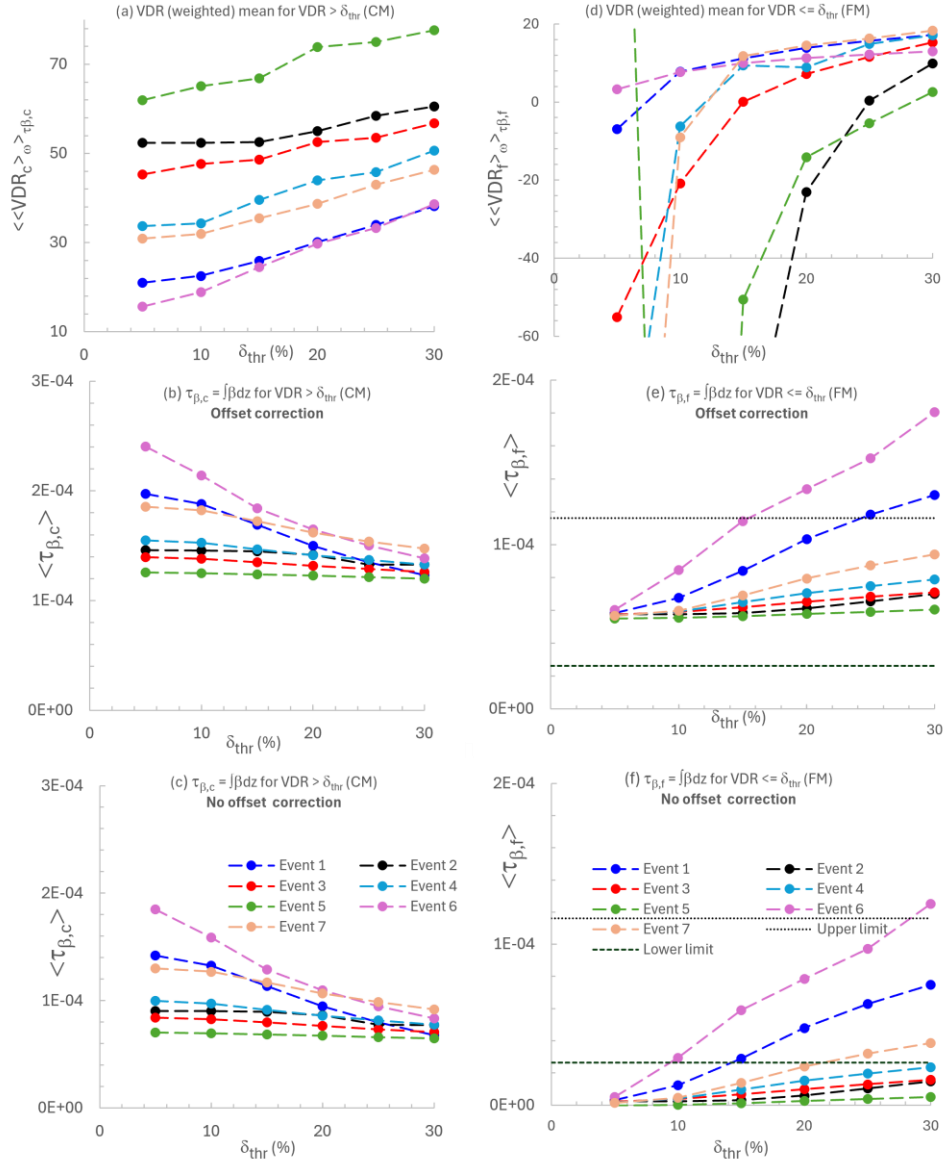
---

<sup>59</sup> we could have reduced that variance with an appropriate smoothing approach but decided to forgo that added complication by the simple expedient of choosing the unweighted statistics since those statistics were largely free of the type of extreme VDR variation that one sees in the unweighted VDR means of Events 2, 3, 4, 5 and 7.

<sup>60</sup> to be mathematically precise, those CM event averages (the y axes labels of the LH graphs of Fig. A4) represent  $\langle \langle VDR^{((VDR)_\omega)_{\tau_\beta > \delta_{thr}}} \rangle_\omega \rangle_{\tau_\beta}$  and  $\langle \tau_\beta = \int \beta^{((VDR)_\omega)_{\tau_\beta > \delta_{thr}}} dz \rangle$  where the VDR vs  $\delta_{thr}$  test is applied to each lidar pixel. The RH FM y-axis labels represent  $\langle \langle VDR^{((VDR)_\omega)_{\tau_\beta \leq \delta_{thr}}} \rangle_\omega \rangle_{\tau_\beta}$  and  $\langle \tau_\beta = \int \beta^{((VDR)_\omega)_{\tau_\beta \leq \delta_{thr}}} dz \rangle$

<sup>61</sup> Values which would tend to be moderately larger at 532 nm (see, for example, Table 1 of Mamouri & Ansmann, 2017)

619 The FM VDR averages are significantly more sensitive to  $\delta_{thr}$  changes at smaller values of that parameter. This is due to a  
620 combination of relatively small numbers of VDR pixels being available at small  $\delta_{thr}$  values and the fact that there seemed to  
621 be a small negative bias in the  $\beta$  values. The  $\tau_\beta$  weighting across each event then produces wildly oscillating VDR averages  
622 at  $\delta_{thr}$  values of 5 and 10% (Event 2, 3, 4, 5 and 7 cases of Fig. A4d) that were enhanced by the very small  $\tau_\beta$  weights in the  
623 denominator of the weighting expression. The small negative bias was the cause of unrealistically small  $\tau_{\beta,f}$  values for the  
624  $\delta_{thr} = 5\%$  case in Fig. A4f. Adding a small  $\beta$  offset to all the  $\beta$  values produced the more realistic “Offset correction” values  
625 of Fig. A4f (values that fit into a range of expected  $\tau_{\beta,f}$  values between the horizontal dotted lines; see the caption of Fig. A4  
626 for further details).



627

628

629

630

631

**Figure A4 – VDR averaged results as a function of  $\delta_{thr}$  for our 7 dust events. LH graphs (CM<sup>62</sup> for VDR values  $> \delta_{thr}$ ): (a) Altitude- and event-averaged  $VDR_c$  values (b)  $\tau_{\beta,c}$  values with offset correction and (c)  $\tau_{\beta,c}$  with no offset correction. RH graphs (d, e, f): the same array of graphs as the left-hand side but for the FM (VDR values  $\leq \delta_{thr}$ ). The “offset correction” was a constant offset added on to  $\beta_c$  and  $\beta_f$  values to eliminate weakly negative  $\beta$  values (due, we presume, to a small calibration inconsistency). The “Lower**

<sup>62</sup> the CM component of the “binary” model defined in Section A2 above

632 limit” and “Upper limit” are roughly-estimated expected bounds<sup>63</sup> on  $\tau_{\beta,f}(0, L)$  (the FM backscatter optical depth across L). These  
 633 statistics were computed for the lidar altitude range from 7.5 to 615 m (a more extensive range than that which was reported in the  
 634 legend of Fig. A2; tests showed that the averaged VDR values were very similar in the face of such small changes in the profile  
 635 range).

Event #	PDR(%)	$\sigma(\text{PDR})$ (%)
1	21	6
2	52	11
3	45	12
4	34	10
5	62	21
6	16	5
7	31	9

636  
 637 **Table A1 – Dust PDRs for our 7 dust events ( $\delta_{thr} = 5\%$ ). The event colors are consistent with Fig. A4. The precision estimates are**  
 638 **event-averaged, intra profile standard deviations discussed in Section A3.2**

639 **A4: Does it help to perform a ( $\omega$ ) weighted CM and FM classification?**

640 If the VDR is so noisy that it requires weighting in the production of altitude-averaged VDRs then the question arises as to  
 641 the variability of the VDR-dependent classification of CM and FM aerosols. An approach, which is arguably coherent with  
 642 our VDR (residual error) weighting scheme, is to associate the VDR weights (which could be thought of as a “number of  
 643 virtual pixels” that increase the importance attributed to a given lidar pixel). Our unweighted FM / CM backscatter AOD  
 644 separation is, for the  $J^{th}$  lidar-profile at time  $t_{i,J}$ ;

645  
 646 
$$\tau_{\beta_c} = \left( \sum_i \beta_{i,J}^{VDR_{i,J} \geq \delta_{thr}} \right) \Delta z \text{ and } \tau_{\beta_f} = \left( \sum_i \beta_{i,J}^{VDR_{i,J} < \delta_{thr}} \right) \Delta z \text{ where } \tau_{\beta_c} + \tau_{\beta_f} = \tau_{\beta} \quad (\text{A5})$$

647  
 648 This equation explicitly indicates that the  $\beta_{i,J}$  summations are mutually exclusive and carried out over all altitude bins of a  
 649 given lidar profile. A weighted version of the FM and CM backscatter ODs for lidar profile  $J^{64}$ , is<sup>65</sup>,

650  
 651 
$$\tau_{\beta_c}^{\omega} = K_J \left[ \sum_i \omega_{i,J} \beta_{i,J} \right]^{VDR_{i,J} \geq \delta_{thr}} \Delta z \text{ and } \tau_{\beta_f}^{\omega} = K_J \left[ \sum_i \omega_{i,J} \beta_{i,J} \right]^{VDR_{i,J} < \delta_{thr}} \Delta z \text{ where } \tau_{\beta}^{\omega} = \tau_{\beta_c}^{\omega} + \tau_{\beta_f}^{\omega} \quad (\text{A6})$$

<sup>63</sup> The extremes of OPAL values of  $\tau_f^0$  computed for each event using a Eureka (experience-based) estimate of the optically active FM lidar backscatter region (~ 5 to 11 km) and the 0.615 km value of L (the atmospheric layer between OPAL and PEARL).

<sup>64</sup> that takes into account the fact that all parameters (those enclosed in the square brackets) must be restricted by the FM and CM conditions

<sup>65</sup> where  $\omega_{i,J}$  is the  $1/RE^2$  weighting defined above

652

653 We then force the relation  $\tau_{\beta c}^{\omega} + \tau_{\beta f}^{\omega} t o = \tau_{\beta}$  (this simply means that  $K_J$  is set to  $\tau_{\beta}/\tau_{\beta}^{\omega}$ ). Dividing both sides by  $\tau_{\beta}$  yields a  
 654 familiar-looking CMF, FMF (CM fraction, FM fraction) type of relation:

655

$$656 \quad CMF^{\omega} + FMF^{\omega} = 1 \text{ where}^{66} \quad (A7a)$$

657

$$658 \quad CMF^{\omega} = \tau_{\beta c}^{\omega}/\tau_{\beta} \text{ and so } \tau_{\beta c}^{\omega} = \tau_{\beta} CMF^{\omega} \quad (A7b)^{67}$$

659

$$660 \quad FMF^{\omega} = \tau_{\beta f}^{\omega}/\tau_{\beta} \text{ and so } \tau_{\beta f}^{\omega} = FMF^{\omega}\tau_{\beta} \quad (A7c)$$

661

662 The  $\tau_{\beta}^{\omega} = \tau_{\beta}$  forcing guarantees that the lidar-profile-integrated differences of  $\Delta\tau_{\beta f} = \langle \tau_{\beta f} - \tau_{\beta f}^{\omega} \rangle$  and  $\Delta\tau_{\beta c} = \langle \tau_{\beta c} - \tau_{\beta c}^{\omega} \rangle$   
 663 of each profile cancel each other out ( $\Delta\tau_{\beta f} + \Delta\tau_{\beta c} = 0$ ).

664 The results shown in Fig. A5 indicate that the “ $\omega$ ” weighting can effectively incite what we attribute to artificial  $\Delta\tau_{\beta c}$  and  
 665  $\Delta\tau_{\beta f}$  spikes<sup>68</sup> (the lidar profiles show no corresponding anomalies), These spikes aside, the CM vs FM classification using a  
 666 weighting approach generally showed no significant  $\tau_{\beta c}^{\omega}$  vs  $\tau_{\beta c}$  changes. Accordingly, any attempt to improve the quality of  
 667  $\tau_{\beta c}$  by VDR-noise-based weighting results in either very little change or is the victim of significant outliers generated by the  
 668 VDR weighting. Unlike the VDR weighting approach improvements (indicated by Fig. A2) there appears to be no significant  
 669 advantage in a VDR-based filtering of the CM / FM classification.

670

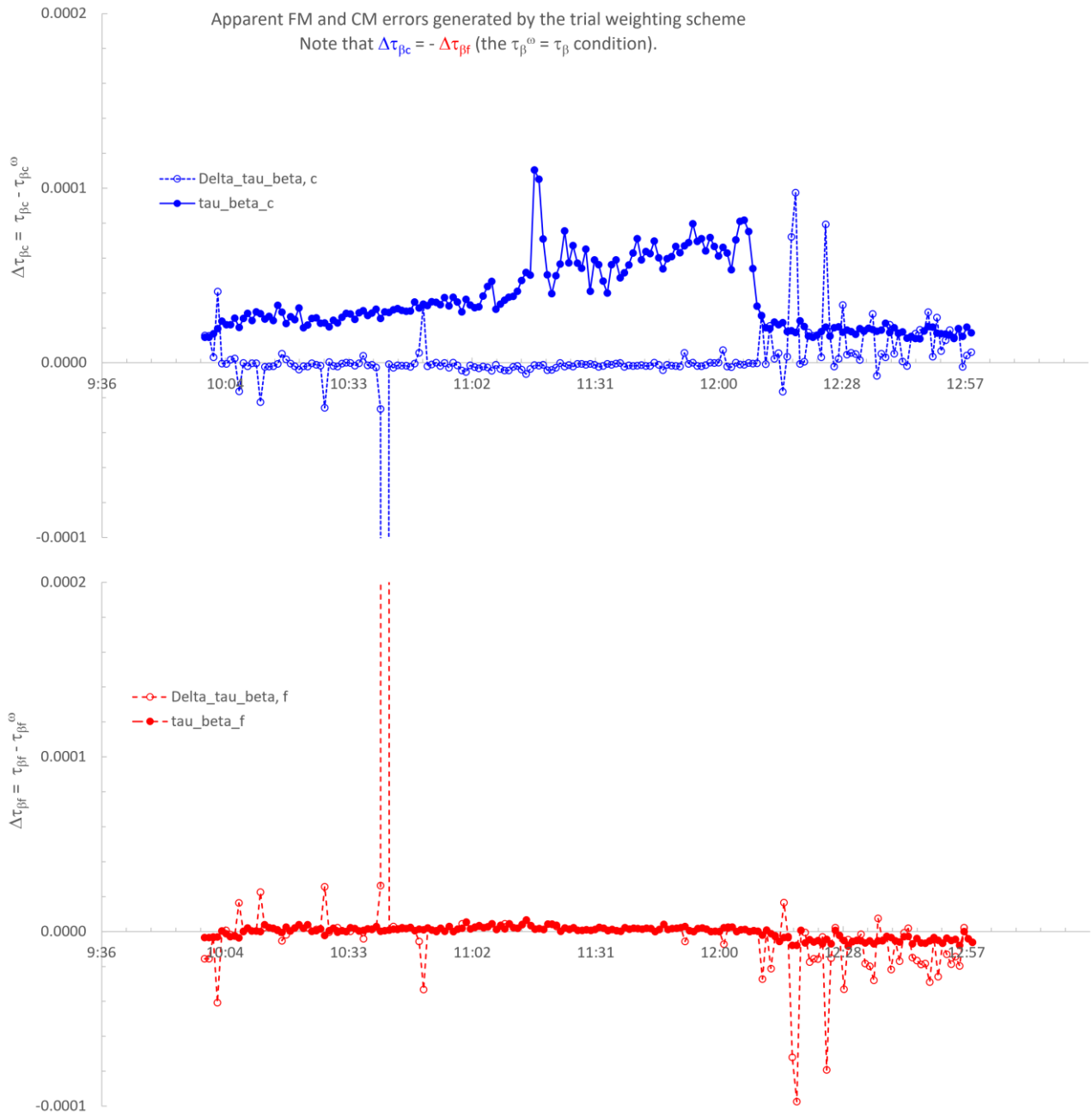
---

<sup>66</sup> Note that  $CMF^{\omega}$  can be  $> 1$  if  $\tau_{\beta c}^{\omega} > \tau_{\beta}$  (negative  $\beta$  values from the real data and attendant underestimates of  $\tau_{\beta}$  can wreak havoc with the “conservation of unity” equation)

<sup>67</sup> A heuristic expression (showing explicitly that  $0 \leq CMF^{\omega} \leq 1$ ) is;

$CMF^{\omega} = \tau_{\beta c}^{\omega}/\tau_{\beta}^{\omega} = [\sum_i \omega_{i,J} \beta_{i,J}]^{VDR_{i,J} \geq \delta_{thr}} \Delta z / \sum_i \omega_{i,J} \beta_{i,J} \Delta z = [\sum_i \omega_{i,J} \beta_{i,J}]^{VDR_{i,J} \geq \delta_{thr}} / \sum_i \omega_{i,J} \beta_{i,J}$ . The explicit link with the unweighted stats is to employ  $\tau_{\beta}$  when calculating  $\tau_{\beta c}^{\omega}$  and  $\tau_{\beta f}^{\omega}$  from  $CMF^{\omega}$ .

<sup>68</sup> The  $\omega_{i,J} \beta_{i,J}$  weighting appears to enhance what would otherwise be nondescript points in the  $\beta_{i,J}$  profile values.



671

672

673

**Figure A5** –  $\Delta\tau_{\beta c} = \langle \tau_{\beta c} - \tau_{\beta c}^{\omega} \rangle$  vs time (top) and (b)  $\Delta\tau_{\beta f} = \langle \tau_{\beta f} - \tau_{\beta f}^{\omega} \rangle$  vs time (example of the July 23, 2007, event).

674 **Appendix B: Acronym and symbol glossary**

675	AERONET: AErosol RObotic NETwork
676	AEROCAN: Canadian sub-network of AERONET
677	AHSRL: Arctic High Spectral Resolution Lidar
678	AOD: Aerosol Optical Depth
679	APS: Aerodynamic Particle Sizer
680	ASL: Above Sea Level
681	CAA: Canadian Arctic Archipelago
682	CARRA: Copernicus Arctic Regional ReAnalysis
683	CALIOP: Cloud-Aerosol Lidar with Orthogonal Polarization
684	CANDAC: Canadian Network for the Detection of Atmospheric Change
685	CM: Coarse Mode
686	CMF: Coarse Mode Fraction (1-FMF)
687	CW: ClockWise
688	CCW: CounterClockWise
689	DB: Deep Blue (MODIS AOD retrieval algorithm over bright surfaces)
690	DT: Dark Target (MODIS AOD retrieval algorithm over dark targets (water and vegetated land))
691	DOD: Dust Optical Depth
692	DR: Depolarisation Ratio
693	ECCC: Environment and Climate Change Canada
694	FM: Fine Mode
695	FMF: Fine Mode Fraction (MODIS product)
696	HLD: High Latitude Dust
697	INP: Ice Nucleating Particle
698	IR: InfraRed
699	KLRS: Kluane Lake Research Station
700	MISR: Multi-angle Imaging SpectroRadiometer
701	MINX: MISR Interactive eXplorer
702	MODIS: Moderate Resolution Imaging Spectroradiometer
703	NA: Not Available
704	NASA: National Aeronautics and Space Administration
705	OD: Optical Depth
706	OPS: Optical Particle Sizer

707 PEARL: Polar Environment Atmospheric Research Laboratory  
708 PDR: Particle Depolarization Ratio  
709 PMSD: Particle-Mass Size Distribution  
710 PVSD: Particle-Volume Size Distribution  
711 R: Correlation Coefficient  
712 RE: Residual Error  
713 RMS: Root Mean Square  
714 RS: Remote Sensing  
715 sr: Steradian  
716 std: Standard Deviation  
717 SWIR: Short-Wave InfraRed  
718 UTC: Coordinated Universal Time  
719 UV: UltraViolet  
720 VDR: Volume Depolarization Ratio  
721 WMO: World Meteorological Organization  
722  $\beta$ : Backscatter Coefficient  
723  $\beta_c$ : CM Backscatter Coefficient  
724  $\tau_\beta$ : Particulate Backscatter Optical Depth  
725  $\tau_{\beta,c}$ : CM  $\tau_\beta$   
726  $\tau_{\beta,f}$ : FM  $\tau_\beta$   
727  $\tau_c^l$ : Lidar CM AOD  
728  $\tau_f^l$ : Lidar FM AOD  
729  $\tau_c^o$ : OPAL CM AOD  
730  $\tau_{c,1.5}^o$ : OPAL cloud-screened (L 1.5) CM AOD  
731  $\tau_c^p$ : PEARL CM AOD  
732  $\tau_{c,1.5}^p$ : PEARL cloud-screened (L 1.5) CM AOD  
733  $S_c$ : CM Lidar Ratio  
734  $S_f$ : FM Lidar Ratio  
735  $v_c$ : Particle-Volume Concentration  
736  $\delta_c$ : CM PDR  
737  $\delta_f$ : FM PDR  
738  $\delta_{thr}$ : VDR threshold

739  $\Delta\tau_c$ : OPAL minus PEARL CM AOD difference ( $\tau_c^O - \tau_c^P$ )

740  $ws$ : Wind Speed (km / h)

741 OPAL: Zero Altitude PEARL Auxiliary Laboratory

## 742 **6 Code availability**

743 MATLAB codes employed for computations reported in this manuscript can be obtained from Seyed Ali Sayedain  
744 ([seyed.ali.sayedain@usherbrooke.ca](mailto:seyed.ali.sayedain@usherbrooke.ca)).

## 745 **7 Data availability**

746 AERONET data are available for download at <https://doi.org/10.17616/R3VK9T> (Lind and Gupta, 2023). The PEARL  
747 AHSRL data are accessible from the University of Wisconsin HSRL data archives at  
748 [https://hsrl.ssec.wisc.edu/by\\_site/2/bscat/2007/07/](https://hsrl.ssec.wisc.edu/by_site/2/bscat/2007/07/) (last accessed: 2025-12-02). APS data can be obtained from Seyed Ali  
749 Sayedain ([seyed.ali.sayedain@usherbrooke.ca](mailto:seyed.ali.sayedain@usherbrooke.ca)). ECCC hourly climate data for different stations can be downloaded at  
750 <https://climate-change.canada.ca/climate-data/#/hourly-climate-data> (last accessed: 2025-12-02). MODIS Terra and Aqua  
751 images and products along with MISR datasets can be downloaded from the Earth Science Data Systems (ESDS) at  
752 <https://search.earthdata.nasa.gov/search>. Sentinel-2 data can be downloaded from Copernicus Browser  
753 (<https://browser.dataspace.copernicus.eu/>). CARRA data at different levels (single, pressure, height and model) can be  
754 downloaded from the Copernicus Climate Data Store (CDS) at <https://cds.climate.copernicus.eu/datasets>.

## 755 **8 Supplement**

756 The supplement related to this article is available online at: <https://doi.org/10.5281/zenodo.20561203> (Sayedain and O'Neill,  
757 2025).

## 758 **9 Author contribution**

759 **Seyed Ali Sayedain:** Writing – original draft preparation – review & editing, Visualization, Investigation, Conceptualization,  
760 Methodology, Formal analysis, Data curation, Validation, Software, Resources. **Norman T. O’Neill:** Writing – review &  
761 editing, Supervision, Visualization, Conceptualization, Methodology, Formal analysis, Data curation, Validation, Funding  
762 acquisition, Resources. **Keyvan Ranjbar:** Review & editing, Data curation, Resources. **Phillipe Gauvin-Bourdon:** Review  
763 & editing, Data curation, Validation. **Rachel Chang:** Review & editing, Data curation, Validation, Funding acquisition,

764 Resources. **Patrick L. Hayes:** Review & editing, Data curation, Validation, Funding acquisition, Resources. **James King:**  
765 Review & editing, Data curation, Validation, Funding acquisition.

## 766 **10 Competing interests**

767 The authors declare that they have no conflict of interest.

## 768 **11 Acknowledgements**

769 Valuable in-kind support was provided by the AEROCAN network of Environment and Climate Change Canada (ECCC), the  
770 NASA AERONET network, the Canada Research Chairs Program (CRC), and the Canadian Network for the Detection of  
771 Atmospheric Change (PAHA/CANDAC) team. We also acknowledge the use of imagery from the NASA Worldview  
772 application (<https://worldview.earthdata.nasa.gov>), part of the NASA Earth Science Data and Information System (ESDIS).  
773 We also acknowledge the use of Sentinel-2 data from the Copernicus Programme and MISR data provided by NASA. We  
774 thank ESA and NASA for making these remote-sensing datasets freely accessible.

## 775 **12 Financial support**

776 was provided by the Discovery Grant (DG) program of the Natural Sciences and Engineering Research Council of Canada  
777 (grant nos. RGPIN-2023-04943, RGPIN-2022-03785, RGPIN-2022-04963), the Canada Research Chairs Program (CRC-  
778 2020-00285) and the SACIA-2 (Signatures of Aerosol-Cloud Interaction over the Arctic) project funded by the Canadian  
779 Space Agency's ESS-DA (Earth System Science – Data Analysis) program (grant no. 21SUASACOA). SACIA-2 is a  
780 collaborative project with Dalhousie University and the Université de Montréal.

## 781 **References**

782 AboEl-Fetouh, Y., O'Neill, N. T., Ranjbar, K., Hesaraki, S., Abboud, I., & Sobolewski, P. S.: Climatological-Scale  
783 Analysis of Intensive and Semi-intensive Aerosol Parameters Derived From AERONET Retrievals Over the Arctic. *Journal*  
784 *of Geophysical Research: Atmospheres*, 125(10). <https://doi.org/10.1029/2019jd031569>, 2020.

785 Arnalds, O.: Dust sources and deposition of aeolian materials in Iceland. *Icelandic Agricultural Sciences*, 23, 3–21.  
786 [https://www.moldin.net/uploads/3/9/3/3/39332633/olafur\\_arnalds\\_2010\\_ias.pdf](https://www.moldin.net/uploads/3/9/3/3/39332633/olafur_arnalds_2010_ias.pdf) (accessed: 2025-11-22), 2010.

787 Adams, P., & Dunbar, M.: Arctic Archipelago. In *The Canadian Encyclopedia*. Available at:  
788 <https://www.thecanadianencyclopedia.ca/en/article/arctic-archipelago> (last accessed: 2025-11-22), 2015.

789 Bachelder, J., Cadieux, M., Liu-Kang, C., Lambert, P., Filoche, A., Galhardi, J. A., Hadioui, M., Chaput, A., Bastien-  
790 Thibault, M. P., Wilkinson, K. J., King, J., & Hayes, P. L.: Chemical and microphysical properties of wind-blown dust near  
791 an actively retreating glacier in Yukon, Canada. *Aerosol Science and Technology*, 54(1), 2–20.  
792 <https://doi.org/10.1080/02786826.2019.1676394>, 2020.

793 Baddock, M., Hall, A., Rideout, J., Bryant, R., Bullard, J., & Gassó, S.: Satellite observations of Arctic blowing dust events  
794 >82°N. *Weather*, 1–6. <https://doi.org/10.1002/wea.7617>, 2024.

795 Barford, N. C., Experimental measurements: precision, error and truth, Addison-Wesley Publishing Company, Inc., Don  
796 Mills, Ontario, ISBN 10: 0201003953, ISBN 13: 9780201003956, 1967.

797 Barr, S. L., Wyld, B., McQuaid, J. B., Neely Iii, R. R., & Murray, B. J.: Southern Alaska as a source of atmospheric mineral  
798 dust and ice-nucleating particles, *Sci. Adv.*, 9, eadg3708. <https://doi.org/10.1126/sciadv.adg3708>, 2023.

799 Bullard, J. E., Matthew, B., Tom, B., John, C., Eleanor, D., Diego, G., Santiago, G., Gudrun, G., Richard, H., Robert, M.,  
800 Cheryl, M.-N., Tom, M., Helena, S., & Thorsteinsson, T.: High latitude dust in the Earth system, *Rev. Geophys.*, 54, 447–485.  
801 <https://doi.org/10.1002/2016RG000518>, 2016.

802 Eloranta, E. W., I. A. Razenkova, J. P. Garcia, & J. Hedrick, -, 22nd International Laser Radar Conference, July 12–16,  
803 Matera, Italy, 2004.

804 Dörnbrack, A., Stachlewska, I. S., Ritter, C., & Neuber, R.: Aerosol distribution around Svalbard during intense easterly  
805 winds. *Atmospheric Chemistry and Physics*, 10(4), 1473–1490. <https://doi.org/10.5194/ACP-10-1473-2010>, 2010.

806 Dubovik, O., Holben, B., Eck, T. F., Smirnov, A., Kaufman, Y. J., King, M. D., Tanré, D., & Slutsker I.: Variability of  
807 absorption and optical properties of key aerosol types observed in worldwide locations. *Journal of the atmospheric sciences*.  
808 59(3):590–608. [https://doi.org/10.1175/1520-0469\(2002\)059<0590:VOAAOP>2.0.CO;2](https://doi.org/10.1175/1520-0469(2002)059<0590:VOAAOP>2.0.CO;2), 2002.

809 Esselborn, M., Wirth, M., Fix, A., Weinzierl, B., Rasp, K., Tesche, M., & Petzold, A.: Spatial distribution and optical  
810 properties of Saharan dust observed by airborne high spectral resolution lidar during SAMUM 2006. *Tellus B Chem. Phys.*  
811 *Meteorol.* 61, 131–143. <https://doi.org/10.1111/j.1600-0889.2008.00394.x>, 2009.

812 Garay, M. J., Witek, M. L., Kahn, R. A., Seidel, F. C., Limbacher, J. A., Bull, M. A., Diner, D. J., Hansen, E. G.,  
813 Kalashnikova, O. V., Lee, H., Nastan, A. M., & Yu, Y.: Introducing the 4.4 km spatial resolution Multi-Angle Imaging  
814 SpectroRadiometer (MISR) aerosol product, *Atmos. Meas. Tech.*, 13, 593–628. <https://doi.org/10.5194/amt-13-593-2020>,  
815 2020.

816 Giles, D. M., Sinyuk, A., Sorokin, M. G., Schafer, J. S., Smirnov, A., Slutsker, I., Eck, T. F., Holben, B. N., Lewis, J. R.,  
817 Campbell, J. R., Welton, E. J., Korkin, S. V., & Lyapustin, A. I.: Advancements in the Aerosol Robotic Network (AERONET)  
818 Version 3 database – automated near-real-time quality control algorithm with improved cloud screening for Sun photometer  
819 aerosol optical depth (AOD) measurements, *Atmos. Meas. Tech.*, 12, 169–209. <https://doi.org/10.5194/amt-12-169-2019>,  
820 2019.

821 Groot Zwaaftink, C. D., Grythe, H., Skov, H., & Stohl, A.: Substantial contribution of northern high-latitude sources to  
822 mineral dust in the Arctic, *J. Geophys. Res.*, 121, 13678-13697. <https://doi.org/10.1002/2016JD025482>, 2016.

823 Hansen J. E. and Travis L. D.: Light scattering in planetary atmospheres, *Space science reviews*. 16(4):527-610.  
824 <https://doi.org/10.1007/BF00168069>, 1974.

825 Huang, Y., Adebisi, A. A., Formenti, P., & Kok, J. F.: Linking the different diameter types of aspherical desert dust  
826 indicates that models underestimate coarse dust emission. *Geophysical Research Letters*, 48, e2020GL092054.  
827 <https://doi.org/10.1029/2020GL092054>, 2021.

828 Justice, C. O., Townshend, J. R. G., Vermote, E. F., Masuoka, E., Wolfe, R. E., Saleous, N., Roy, D. P., & Morisette, J. T.:  
829 An overview of MODIS Land data processing and product status. *Remote Sensing of Environment*, 83(1–2), 3–15.  
830 [https://doi.org/10.1016/S0034-4257\(02\)00084-6](https://doi.org/10.1016/S0034-4257(02)00084-6), 2002.

831 Kahn, R. A., Li, W.-H., Moroney, C., Diner, D. J., Martonchik, J. V., & Fishbein, E.: Aerosol source plume physical  
832 characteristics from space-based multiangle imaging, *Journal of Geophysical Research Atmospheres*, 112, D11205.  
833 <https://doi.org/10.1029/2006JD007647>, 2007.

834 Kaltschmitt, M., Streicher, W., & Wiese, A.: *Renewable Energy – Technology, Economics and Environment (XXXII)*.  
835 Berlin, Heidelberg, New York, Springer. ISBN 3-540-70947-9, ISBN 978-3-540-70947-3, Page 55. Available at:  
836 <http://www.springer.com/us/book/9783540709473> (last accessed: 2025-11-22), 2007.

837 Kawai, K., Matsui, H., & Tobo, Y.: Dominant Role of Arctic Dust With High Ice Nucleating Ability in the Arctic Lower  
838 Troposphere. *Geophysical Research Letters*, 50(8), 1–10. <https://doi.org/10.1029/2022GL102470>, 2023.

839 Lesins, G., Duck, T. J., & Drummond, J. R.: Climate trends at Eureka in the Canadian high arctic. *Atmosphere-*  
840 *Ocean*, 48(2), 59–80. <https://doi.org/10.3137/AO1103.2010>, 2010.

841 Levy, R., Hsu, C., et al., : MODIS Atmosphere L2 Aerosol Product. NASA MODIS Adaptive Processing System, Goddard  
842 Space Flight Center, USA: [http://dx.doi.org/10.5067/MODIS/MOD04\\_3K.061](http://dx.doi.org/10.5067/MODIS/MOD04_3K.061), 2015a.

843 Levy, R., Hsu, C., et al.,: MODIS Atmosphere L2 Aerosol Product. NASA MODIS Adaptive Processing System, Goddard  
844 Space Flight Center, USA: [http://dx.doi.org/10.5067/MODIS/MYD04\\_3K.061](http://dx.doi.org/10.5067/MODIS/MYD04_3K.061), 2015b.

845 Levy, R., Hsu, C., et al., : MODIS Atmosphere L2 Aerosol Product. NASA MODIS Adaptive Processing System, Goddard  
846 Space Flight Center, USA: [http://dx.doi.org/10.5067/MODIS/MOD04\\_L2.061](http://dx.doi.org/10.5067/MODIS/MOD04_L2.061), 2015c.

847 Levy, R., Hsu, C., et al.,: MODIS Atmosphere L2 Aerosol Product. NASA MODIS Adaptive Processing System, Goddard  
848 Space Flight Center, USA: [http://dx.doi.org/10.5067/MODIS/MYD04\\_L2.061](http://dx.doi.org/10.5067/MODIS/MYD04_L2.061), 2015d.

849 Lind, E. and Gupta, P.: AERONET, Registry of Research Data Repositories [data set], <https://doi.org/10.17616/R3VK9T>  
850 (last accessed: 2025-12-02), 2023.

851 Liu, Z., Fairlie, T. D., Uno, I., Huang, J., Wu, D., Omar, A., Kar, J., Vaughan, M., Rogers, R., Winker, D., Trepte, C., Hu,  
852 Y., Sun, W., Lin, B., & Cheng, A.: Transpacific transport and evolution of the optical properties of Asian dust, *Journal of*  
853 *Quantitative Spectroscopy & Radiative Transfer*, 116, 24–33. <https://doi.org/10.1016/j.jqsrt.2012.11.011>, 2013.

854 Mamouri, R. E. & Ansmann, A.: Fine and coarse dust separation with polarization lidar, *Atmos. Meas. Tech.*, 7, 3717–  
855 3735. <https://doi.org/10.5194/amt-7-3717-2014>, 2014.

856 Mamouri, R. E. & Ansmann, A.: Potential of polarization/Raman lidar to separate fine dust, coarse dust, maritime, and  
857 anthropogenic aerosol profiles, *Atmos. Meas. Tech.*, 10, 3403–3427. <https://doi.org/10.5194/amt-10-3403-2017>, 2017.

858 Martonchik, J. V., Diner, D. J., Kahn, R. A., Ackerman, T. P., Verstraete, M. M., Pinty, B., & Gordon, H. R.: Techniques  
859 for the retrieval of aerosol properties over land and ocean using multiangle imaging. *IEEE Transactions on Geoscience and*  
860 *Remote Sensing*, 36(4), 1212–1227. <https://doi.org/10.1109/36.701027>, 1998.

861 Meinander, O., Dagsson-Waldhauserova, P., Amosov, P., Aseyeva, E., Atkins, C., Baklanov, A., Baldo, C., Barr, S. L.,  
862 Barzycka, B., Benning, L. G., Cvetkovic, B., Enchilik, P., Frolov, D., Gassó, S., Kandler, K., Kasimov, N., Kavan, J., King,  
863 J., Koroleva, T., Krupskaya, V., Kulmala, M., Kusiak, M., Lappalainen, H. K., Laska, M., Lasne, J., Lewandowski, M., Luks,  
864 B., McQuaid, J. B., Moroni, B., Murray, B., Möhler, O., Nawrot, A., Nickovic, S., O’Neill, N. T., Pejanovic, G., Popovicheva,  
865 O., Ranjbar, K., Romanias, M., Samonova, O., Sanchez-Marroquin, A., Schepanski, K., Semenov, I., Sharapova, A.,  
866 Shevnina, E., Shi, Z., Sofiev, M., Thevenet, F., Thorsteinsson, T., Timofeev, M., Umo, N. S., Uppstu, A., Urupina, D., Varga,  
867 G., Werner, T., Arnalds, O., & Vukovic Vimic, A.: Newly identified climatically and environmentally significant high-latitude  
868 dust sources. *Atmospheric Chemistry and Physics*, 22(17), 11889–11930. <https://doi.org/10.5194/acp-22-11889-2022>, 2022.

869 Met Office, Beaufort, National Meteorological Library and Archive, Fact sheet 6 – The Beaufort Scale. Available at:  
870 <https://www.metoffice.gov.uk/binaries/content/assets/metofficegovuk/pdf/research/library-and->  
871 [archive/library/publications/factsheets/factsheet\\_6-the-beaufort-scale\\_2023.pdf](https://www.metoffice.gov.uk/binaries/content/assets/metofficegovuk/pdf/research/library-and-archive/library/publications/factsheets/factsheet_6-the-beaufort-scale_2023.pdf) (last accessed: 2025-11-22), 2010.

872 Mishchenko, M. I., & Sassen, K.: Depolarization of lidar returns by small ice crystals: An application to contrails,  
873 *Geophysical Research Letters*, 25(3), 309–312. <https://doi.org/10.1029/97GL03764>, 1998.

874 MISR Handbook: Multi-angle Imaging SpectroRadiometer Project Handbook, *Atmospheric Science Data Center*, NASA  
875 Langley Research Center. Available at: [https://asdc.larc.nasa.gov/documents/misr/guide/misr\\_ov2.pdf](https://asdc.larc.nasa.gov/documents/misr/guide/misr_ov2.pdf) (last accessed: 2024-  
876 12-21), 2000.

877 Nelson, D. L., Garay, M. J., Kahn, R. A., & Dunst, B. A.: Stereoscopic height and wind retrievals for aerosol plumes with  
878 the MISR INteractive eXplorer (MINX). *Remote Sensing*, 5(9), 4593–4628. <https://doi.org/10.3390/rs5094593>, 2013.

879 O’Neill, N. T., Ranjbar, K., Ivănescu, L., Blanchard, Y., Sayedain, S. A., & AboEl-Fetouh, Y.: Remote-sensing  
880 detectability of airborne Arctic dust, *Atmos. Chem. Phys.*, 25, 27–44, <https://doi.org/10.5194/acp-25-27-2025>, 2025.

881 Ranjbar, K., O’Neill, N. T., Ivanescu, L., King, J., & Hayes, P. L.: Remote sensing of a high-Arctic, local dust event over  
882 Lake Hazen (Ellesmere Island, Nunavut, Canada). *Atmospheric Environment*, 246, 118102.  
883 <https://doi.org/10.1016/j.atmosenv.2020.118102>, 2021.

884 Remer, L. A., Mattoo, S., Levy, R. C., & Munchak, L. A.: MODIS 3 km aerosol product: algorithm and global perspective,  
885 *Atmos. Meas. Tech.*, 6, 1829–1844. <https://doi.org/10.5194/amt-6-1829-2013>, 2013.

886 Sayedain, S. A., O'Neill, N. T., King, J., Hayes, P. L., Bellamy, D., Washington, R., Engelstaedter, S., Vicente-Luis, A.,  
887 Bachelder, J., & Bernhard, M.: Detection and analysis of Lhù'àn Man' (Kluane Lake) dust plumes using passive and active  
888 ground-based remote sensing supported by physical surface measurements. *Atmospheric Measurement Techniques*, 16(17),  
889 4115–4135. <https://doi.org/10.5194/amt-16-4115-2023>, 2023.

890 Sayedain, S. A., & O'Neill, N. T.: Remote sensing of local-dust across the Canadian Arctic - Supplementary Material. In  
891 *Atmospheric Measurement Techniques*. Zenodo. <https://doi.org/10.5281/zenodo.20561203>, 2026.

892 Sayer, A. M., Munchak, L. A., Hsu, N. C., Levy, R. C., Bettenhausen, C., & Jeong, M.-J.: MODIS Collection 6 aerosol  
893 products: Comparison between Aqua's e-Deep Blue, Dark Target, and “merged” data sets, and usage recommendations,  
894 *Journal of Geophysical Research: Atmospheres*, 119, 13,965–13,989. <https://doi.org/10.1002/2014JD022453>, 2014.

895 Sayer, A., Personal communication, 2025.

896 Sinyuk, A., Holben, B. N., Eck, T. F., Giles, D. M., Slutsker, I., Korkin, S., Schafer, J. S., Smirnov, A., Sorokin, M., &  
897 Lyapustin, A.: The AERONET Version 3 aerosol retrieval algorithm, associated uncertainties and comparisons to Version 2.  
898 *Atmospheric Measurement Techniques*. Jun 26;13(6):3375-411. <https://doi.org/10.5194/amt-13-3375-2020>, 2020.

899 Song, Q., Zhang, Z., Yu, H., Ginoux, P., & Shen, J.: Global dust optical depth climatology derived from CALIOP and  
900 MODIS aerosol retrievals on decadal timescales: regional and interannual variability, *Atmos. Chem. Phys.*, 21, 13369–13395.  
901 <https://doi.org/10.5194/acp-21-13369-2021>, 2021.

902 Tian, Y., Pan, X., Wang, Z., Wang, D., Ge, B., Liu, X., Zhang, Y., Liu, H., Lei, S., Yang, T., Fu, P., Sun, Y., & Wang, Z.:  
903 Transport patterns, size distributions, and depolarization characteristics of dust particles in East Asia in spring 2018, *Journal*  
904 *of Geophysical Research: Atmospheres*, 125(16):e2019JD031752. <https://doi.org/10.1029/2019JD031752>, 2020.

905 Tobo, Y., Adachi, K., DeMott, P. J., Hill, T. C. J., Hamilton, D. S., Mahowald, N. M., Nagatsuka, N., Ohata, S., Uetake,  
906 J., Kondo, Y., & Koike, M.: Glacially sourced dust as a potentially significant source of ice nucleating particles. *Nature*  
907 *Geoscience*, 12(4), 253–258. <https://doi.org/10.1038/s41561-019-0314-x>, 2019.

908 TSI Incorporated, *Aerodynamic Particle Sizer® (APSTM) Model 3321* [Specification sheet]. Available at:  
909 <https://www.tsi.com/getmedia/7fd20aa0-8540-4b8d-8572-d164366dd08c/3321-Spec-Sheet-US?ext=.pdf> (last accessed:  
910 2025-01-11), 2022.

911 Uno, I., Eguchi, K., Yumimoto, K., Takemura, T., Shimizu, A., Uematsu, M., Liu, Z., Wang, Z., Hara, Y., & Sugimoto,  
912 N.: Asian dust transported one full circuit around the globe. *Nature Geoscience*, 2(8), 557–560.  
913 <https://doi.org/10.1038/ngeo583>, 2009.

914 Weitkamp, C.: *Lidar: range-resolved optical remote sensing of the atmosphere*, Springer Science & Business Media, New  
915 York (HSRL chapter 5 by E. Eloranta), 2005.

916 Williamson, M. -C. & MacRae, R. A.: Mineralization potential in volcanic rocks of the Strand Fiord Formation and  
917 associated intrusions, Axel Heiberg Island, Nunavut, Canada. Geological Survey of Canada, Open File, 7981, 34. Natural  
918 Resources Canada. <https://doi.org/10.4095/297365>, 2015.

919 Witek, M. L., Garay, M. J., Diner, D. J., Bull, M. A., Seidel, F. C., Nastan, A. M., & Hansen, E. G.: Introducing the MISR  
920 level 2 near real-time aerosol product. *Atmospheric Measurement Techniques*, 14(8), 5577–5591. <https://doi.org/10.5194/amt-14-5577-2021>, 2021.

922 Woo, M. K., Edlund, S. A., & Young, K. L.: Occurrence of early snow-free zones on Fosheim Peninsula, Ellesmere Island,  
923 Northwest Territories. *Current Research, Part B, Geological Survey of Canada Paper*, 91, 9-14, ISBN: 0-660-56282-0.  
924 Available at: [https://publications.gc.ca/collections/collection\\_2017/rncan-nrcan/M44-91-1B.pdf](https://publications.gc.ca/collections/collection_2017/rncan-nrcan/M44-91-1B.pdf) (last accessed: 2025-11-22),  
925 1991.

926 Xi, Y., Xu, C., Downey, A., Stevens, R., Bachelder, J. O., King, J., Hayes, P. L., & Bertram, A. K.: Ice nucleating properties  
927 of airborne dust from an actively retreating glacier in Yukon, Canada. *Environmental Science: Atmospheres*, 2(4), 714–726.  
928 <https://doi.org/10.1039/d1ea00101a>, 2022.

929 Yang, S., Preißler, J., Wiegner, M., von Löwis, S., Petersen, G. N., Parks, M. M., & Finger, D. C.: Monitoring dust events  
930 using doppler lidar and ceilometer in Iceland. *Atmosphere*, 11(12), 1–23. <https://doi.org/10.3390/atmos11121294>, 2020.

931 Zhao, X., Huang, K., Fu, J. S., & Abdullaev, S. F.: Long-range transport of Asian dust to the Arctic: identification of  
932 transport pathways, evolution of aerosol optical properties, and impact assessment on surface albedo changes. *Atmospheric  
933 Chemistry and Physics*, 22(15), 10389–10407. <https://doi.org/10.5194/acp-22-10389-2022>, 2022.